

Measurements of the $B \rightarrow D^*$ Form Factors Using the Decay $\bar{B}^0 \rightarrow D^{*+} e^- \bar{\nu}_e$

B. Aubert, R. Barate, D. Boutigny, F. Couderc, Y. Karyotakis, J. P. Lees, V. Poireau, V. Tisserand, and A. Zghiche
Laboratoire de Physique des Particules, F-74941 Annecy-le-Vieux, France

E. Grauges
IFAE, Universitat Autònoma de Barcelona, E-08193 Bellaterra, Barcelona, Spain

A. Palano and M. Pappagallo
Università di Bari, Dipartimento di Fisica and INFN, I-70126 Bari, Italy

J. C. Chen, N. D. Qi, G. Rong, P. Wang, and Y. S. Zhu
Institute of High Energy Physics, Beijing 100039, China

G. Eigen, I. Ofte, and B. Stugu
University of Bergen, Institute of Physics, N-5007 Bergen, Norway

G. S. Abrams, M. Battaglia, D. S. Best, D. N. Brown, J. Button-Shafer, R. N. Cahn,
E. Charles, C. T. Day, M. S. Gill, A. V. Gritsan,* Y. Groysman, R. G. Jacobsen, R. W. Kadel,
J. A. Kadyk, L. T. Kerth, Yu. G. Kolomensky, G. Kukartsev, G. Lynch, L. M. Mir,
P. J. Oddone, T. J. Orimoto, M. Pripstein, N. A. Roe, M. T. Ronan, and W. A. Wenzel
Lawrence Berkeley National Laboratory and University of California, Berkeley, California 94720, USA

M. Barrett, K. E. Ford, T. J. Harrison, A. J. Hart, C. M. Hawkes, S. E. Morgan, and A. T. Watson
University of Birmingham, Birmingham, B15 2TT, United Kingdom

M. Fritsch, K. Goetzen, T. Held, H. Koch, B. Lewandowski, M. Pelizaeus, K. Peters, T. Schroeder, and M. Steinke
Ruhr Universität Bochum, Institut für Experimentalphysik 1, D-44780 Bochum, Germany

J. T. Boyd, J. P. Burke, W. N. Cottingham, and D. Walker
University of Bristol, Bristol BS8 1TL, United Kingdom

T. Cuhadar-Donszelmann, B. G. Fulsom, C. Hearty, N. S. Knecht, T. S. Mattison, and J. A. McKenna
University of British Columbia, Vancouver, British Columbia, Canada V6T 1Z1

A. Khan, P. Kyberd, M. Saleem, and L. Teodorescu
Brunel University, Uxbridge, Middlesex UB8 3PH, United Kingdom

V. E. Blinov, A. D. Bukin, V. P. Druzhinin, V. B. Golubev, E. A. Kravchenko,
A. P. Onuchin, S. I. Serebnyakov, Yu. I. Skovpen, E. P. Solodov, and K. Yu Todyshev
Budker Institute of Nuclear Physics, Novosibirsk 630090, Russia

M. Bondioli, M. Bruinsma, M. Chao, S. Curry, I. Eschrich, D. Kirkby, A. J. Lankford,
P. Lund, M. Mandelkern, R. K. Mommsen, W. Roethel, and D. P. Stoker
University of California at Irvine, Irvine, California 92697, USA

S. Abachi and C. Buchanan
University of California at Los Angeles, Los Angeles, California 90024, USA

S. D. Foulkes, J. W. Gary, O. Long, B. C. Shen, K. Wang, and L. Zhang
University of California at Riverside, Riverside, California 92521, USA

D. del Re, H. K. Hadavand, E. J. Hill, H. P. Paar, S. Rahatlou, and V. Sharma
University of California at San Diego, La Jolla, California 92093, USA

J. W. Berryhill, C. Campagnari, A. Cunha, B. Dahmes, T. M. Hong, and J. D. Richman
University of California at Santa Barbara, Santa Barbara, California 93106, USA

T. W. Beck, A. M. Eisner, C. J. Flacco, C. A. Heusch, J. Kroseberg, W. S. Lockman, G. Nesom,
 T. Schalk, B. A. Schumm, A. Seiden, P. Spradlin, D. C. Williams, and M. G. Wilson
University of California at Santa Cruz, Institute for Particle Physics, Santa Cruz, California 95064, USA

J. Albert, E. Chen, G. P. Dubois-Felsmann, A. Dvoretzkii, D. G. Hitlin,
 J. S. Minamora, I. Narsky, T. Piatenko, F. C. Porter, A. Ryd, and A. Samuel
California Institute of Technology, Pasadena, California 91125, USA

R. Andreassen, G. Mancinelli, B. T. Meadows, and M. D. Sokoloff
University of Cincinnati, Cincinnati, Ohio 45221, USA

F. Blanc, P. C. Bloom, S. Chen, W. T. Ford, J. F. Hirschauer, A. Kreisel, U. Nauenberg,
 A. Olivas, W. O. Ruddick, J. G. Smith, K. A. Ulmer, S. R. Wagner, and J. Zhang
University of Colorado, Boulder, Colorado 80309, USA

A. Chen, E. A. Eckhart, A. Soffer, W. H. Toki, R. J. Wilson, F. Winklmeier, and Q. Zeng
Colorado State University, Fort Collins, Colorado 80523, USA

D. D. Altenburg, E. Feltresi, A. Hauke, H. Jasper, and B. Spaan
Universität Dortmund, Institut für Physik, D-44221 Dortmund, Germany

T. Brandt, M. Dickopp, V. Klose, H. M. Lacker, R. Nogowski, S. Otto, A. Petzold,
 J. Schubert, K. R. Schubert, R. Schwierz, J. E. Sundermann, and A. Volk
Technische Universität Dresden, Institut für Kern- und Teilchenphysik, D-01062 Dresden, Germany

D. Bernard, G. R. Bonneaud, P. Grenier,[†] E. Latour, S. Schrenk, Ch. Thiebaux, G. Vasileiadis, and M. Verderi
Ecole Polytechnique, LLR, F-91128 Palaiseau, France

D. J. Bard, P. J. Clark, W. Gradl, F. Muheim, S. Playfer, and Y. Xie
University of Edinburgh, Edinburgh EH9 3JZ, United Kingdom

M. Andreotti, D. Bettoni, C. Bozzi, R. Calabrese, G. Cibinetto, E. Luppi, M. Negrini, and L. Piemontese
Università di Ferrara, Dipartimento di Fisica and INFN, I-44100 Ferrara, Italy

F. Anulli, R. Baldini-Ferrolì, A. Calcaterra, R. de Sangro, G. Finocchiaro,
 S. Pacetti, P. Patteri, I. M. Peruzzi,[‡] M. Piccolo, and A. Zallo
Laboratori Nazionali di Frascati dell'INFN, I-00044 Frascati, Italy

A. Buzzo, R. Capra, R. Contri, M. Lo Vetere, M. M. Macri, M. R. Monge,
 S. Passaggio, C. Patrignani, E. Robutti, A. Santroni, and S. Tosi
Università di Genova, Dipartimento di Fisica and INFN, I-16146 Genova, Italy

G. Brandenburg, K. S. Chaisanguanthum, M. Morii, and J. Wu
Harvard University, Cambridge, Massachusetts 02138, USA

R. S. Dubitzky, J. Marks, S. Schenk, and U. Uwer
Universität Heidelberg, Physikalisches Institut, Philosophenweg 12, D-69120 Heidelberg, Germany

W. Bhimji, D. A. Bowerman, P. D. Dauncey, U. Egede, R. L. Flack,
 J. R. Gaillard, J. A. Nash, M. B. Nikolich, and W. Panduro Vazquez
Imperial College London, London, SW7 2AZ, United Kingdom

X. Chai, M. J. Charles, W. F. Mader, U. Mallik, and V. Ziegler
University of Iowa, Iowa City, Iowa 52242, USA

J. Cochran, H. B. Crawley, L. Dong, V. Eyges, W. T. Meyer, S. Prell, E. I. Rosenberg, and A. E. Rubin
Iowa State University, Ames, Iowa 50011-3160, USA

G. Schott
Universität Karlsruhe, Institut für Experimentelle Kernphysik, D-76021 Karlsruhe, Germany

N. Arnaud, M. Davier, G. Grosdidier, A. Höcker, F. Le Diberder, V. Lepeltier, A. M. Lutz, A. Oyanguren,
 T. C. Petersen, S. Pruvot, S. Rodier, P. Roudeau, M. H. Schune, A. Stocchi, W. F. Wang, and G. Wormser
Laboratoire de l'Accélérateur Linéaire, F-91898 Orsay, France

C. H. Cheng, D. J. Lange, and D. M. Wright
Lawrence Livermore National Laboratory, Livermore, California 94550, USA

A. J. Bevan, C. A. Chavez, I. J. Forster, J. R. Fry, E. Gabathuler, R. Gamet,
 K. A. George, D. E. Hutchcroft, D. J. Payne, K. C. Schofield, and C. Touramanis
University of Liverpool, Liverpool L69 7ZE, United Kingdom

F. Di Lodovico, W. Menges, and R. Sacco
Queen Mary, University of London, E1 4NS, United Kingdom

C. L. Brown, G. Cowan, H. U. Flaecher, M. G. Green, D. A. Hopkins,
 P. S. Jackson, T. R. McMahon, S. Ricciardi, and F. Salvatore
University of London, Royal Holloway and Bedford New College, Egham, Surrey TW20 0EX, United Kingdom

D. N. Brown and C. L. Davis
University of Louisville, Louisville, Kentucky 40292, USA

J. Allison, N. R. Barlow, R. J. Barlow, Y. M. Chia, C. L. Edgar,
 M. P. Kelly, G. D. Lafferty, M. T. Naisbit, J. C. Williams, and J. I. Yi
University of Manchester, Manchester M13 9PL, United Kingdom

C. Chen, W. D. Hulsbergen, A. Jawahery, D. Kovalskiy, C. K. Lae, D. A. Roberts, and G. Simi
University of Maryland, College Park, Maryland 20742, USA

G. Blaylock, C. Dallapiccola, S. S. Hertzbach, R. Kofler, X. Li, T. B. Moore, S. Saremi, H. Staengle, and S. Y. Willocq
University of Massachusetts, Amherst, Massachusetts 01003, USA

R. Cowan, K. Koenek, G. Sciolla, S. J. Sekula, M. Spitznagel, F. Taylor, and R. K. Yamamoto
Massachusetts Institute of Technology, Laboratory for Nuclear Science, Cambridge, Massachusetts 02139, USA

H. Kim, P. M. Patel, C. T. Potter, and S. H. Robertson
McGill University, Montréal, Québec, Canada H3A 2T8

A. Lazzaro, V. Lombardo, and F. Palombo
Università di Milano, Dipartimento di Fisica and INFN, I-20133 Milano, Italy

J. M. Bauer, L. Cremaldi, V. Eschenburg, R. Godang, R. Kroeger,
 J. Reidy, D. A. Sanders, D. J. Summers, and H. W. Zhao
University of Mississippi, University, Mississippi 38677, USA

S. Brunet, D. Côté, P. Taras, and F. B. Viaud
Université de Montréal, Physique des Particules, Montréal, Québec, Canada H3C 3J7

H. Nicholson
Mount Holyoke College, South Hadley, Massachusetts 01075, USA

N. Cavallo,[§] G. De Nardo, F. Fabozzi,[§] C. Gatto, L. Lista, D. Monorchio, P. Paolucci, D. Piccolo, and C. Sciacca
Università di Napoli Federico II, Dipartimento di Scienze Fisiche and INFN, I-80126, Napoli, Italy

M. Baak, H. Bulten, G. Raven, and H. L. Snoek
NIKHEF, National Institute for Nuclear Physics and High Energy Physics, NL-1009 DB Amsterdam, The Netherlands

C. P. Jessop and J. M. LoSecco
University of Notre Dame, Notre Dame, Indiana 46556, USA

T. Allmendinger, G. Benelli, K. K. Gan, K. Honscheid, D. Hufnagel, P. D. Jackson,
 H. Kagan, R. Kass, T. Pulliam, A. M. Rahimi, R. Ter-Antonyan, and Q. K. Wong
Ohio State University, Columbus, Ohio 43210, USA

N. L. Blount, J. Brau, R. Frey, O. Igonkina, M. Lu, R. Rahmat, N. B. Sinev, D. Strom, J. Strube, and E. Torrence
University of Oregon, Eugene, Oregon 97403, USA

F. Galeazzi, M. Margoni, M. Morandin, A. Pompili, M. Posocco, M. Rotondo, F. Simonetto, R. Stroili, and C. Voci
Università di Padova, Dipartimento di Fisica and INFN, I-35131 Padova, Italy

M. Benayoun, J. Chauveau, P. David, L. Del Buono, Ch. de la Vaissière, O. Hamon,
 B. L. Hartfiel, M. J. J. John, Ph. Leruste, J. Malclès, J. Ocariz, L. Roos, and G. Therin
Universités Paris VI et VII, Laboratoire de Physique Nucléaire et de Hautes Energies, F-75252 Paris, France

P. K. Behera, L. Gladney, and J. Panetta
University of Pennsylvania, Philadelphia, Pennsylvania 19104, USA

M. Biasini, R. Covarelli, and M. Pioppi
Università di Perugia, Dipartimento di Fisica and INFN, I-06100 Perugia, Italy

C. Angelini, G. Batignani, S. Bettarini, F. Bucci, G. Calderini, M. Carpinelli, R. Cenci, F. Forti, M. A. Giorgi,
 A. Lusiani, G. Marchiori, M. A. Mazur, M. Morganti, N. Neri, E. Paoloni, M. Rama, G. Rizzo, and J. Walsh
Università di Pisa, Dipartimento di Fisica, Scuola Normale Superiore and INFN, I-56127 Pisa, Italy

M. Haire, D. Judd, and D. E. Wagoner
Prairie View A&M University, Prairie View, Texas 77446, USA

J. Biesiada, N. Danielson, P. Elmer, Y. P. Lau, C. Lu, J. Olsen, A. J. S. Smith, and A. V. Telnov
Princeton University, Princeton, New Jersey 08544, USA

F. Bellini, G. Cavoto, A. D’Orazio, E. Di Marco, R. Faccini, F. Ferrarotto, F. Ferroni, M. Gaspero,
 L. Li Gioi, M. A. Mazzoni, S. Morganti, G. Piredda, F. Polci, F. Safai Tehrani, and C. Voena
Università di Roma La Sapienza, Dipartimento di Fisica and INFN, I-00185 Roma, Italy

H. Schröder and R. Waldi
Universität Rostock, D-18051 Rostock, Germany

T. Adye, N. De Groot, B. Franek, E. O. Olaiya, and F. F. Wilson
Rutherford Appleton Laboratory, Chilton, Didcot, Oxon, OX11 0QX, United Kingdom

S. Emery, A. Gaidot, S. F. Ganzhur, G. Hamel de Monchenault,
 W. Kozanecki, M. Legendre, B. Mayer, G. Vasseur, Ch. Yèche, and M. Zito
DSM/Dapnia, CEA/Saclay, F-91191 Gif-sur-Yvette, France

W. Park, M. V. Purohit, A. W. Weidemann, and J. R. Wilson
University of South Carolina, Columbia, South Carolina 29208, USA

T. Abe, M. T. Allen, D. Aston, R. Bartoldus, N. Berger, A. M. Boyarski, R. Claus, J. P. Coleman,
 M. R. Convery, M. Cristinziani, J. C. Dingfelder, D. Dong, J. Dorfan, D. Dujmic, W. Dunwoodie,
 S. Fan, R. C. Field, T. Glanzman, S. J. Gowdy, T. Hadig, V. Halyo, C. Hast, T. Hryn’ova, W. R. Innes,
 M. H. Kelsey, P. Kim, M. L. Kocian, D. W. G. S. Leith, J. Libby, S. Luitz, V. Luth, H. L. Lynch,

D. B. MacFarlane, H. Marsiske, R. Messner, D. R. Muller, C. P. O'Grady, V. E. Ozcan, A. Perazzo, M. Perl, B. N. Ratcliff, A. Roodman, A. A. Salnikov, R. H. Schindler, J. Schwiening, A. Snyder, J. Stelzer, D. Su, M. K. Sullivan, K. Suzuki, S. K. Swain, J. M. Thompson, J. Va'vra, N. van Bakel, M. Weaver, A. J. R. Weinstein, W. J. Wisniewski, M. Wittgen, D. H. Wright, A. K. Yarritu, K. Yi, and C. C. Young
Stanford Linear Accelerator Center, Stanford, California 94309, USA

P. R. Burchat, A. J. Edwards, S. A. Majewski, B. A. Petersen, C. Roat, and L. Wilden
Stanford University, Stanford, California 94305-4060, USA

S. Ahmed, M. S. Alam, R. Bula, J. A. Ernst, V. Jain, B. Pan, M. A. Saeed, F. R. Wappler, and S. B. Zain
State University of New York, Albany, New York 12222, USA

W. Bugg, M. Krishnamurthy, and S. M. Spanier
University of Tennessee, Knoxville, Tennessee 37996, USA

R. Eckmann, J. L. Ritchie, A. Satpathy, and R. F. Schwitters
University of Texas at Austin, Austin, Texas 78712, USA

J. M. Izen, I. Kitayama, X. C. Lou, and S. Ye
University of Texas at Dallas, Richardson, Texas 75083, USA

F. Bianchi, M. Bona, F. Gallo, and D. Gamba
Università di Torino, Dipartimento di Fisica Sperimentale and INFN, I-10125 Torino, Italy

M. Bomben, L. Bosisio, C. Cartaro, F. Cossutti, G. Della Ricca, S. Dittongo, S. Grancagnolo, L. Lanceri, and L. Vitale
Università di Trieste, Dipartimento di Fisica and INFN, I-34127 Trieste, Italy

V. Azzolini and F. Martinez-Vidal
IFIC, Universitat de Valencia-CSIC, E-46071 Valencia, Spain

R. S. Panvini[¶]
Vanderbilt University, Nashville, Tennessee 37235, USA

Sw. Banerjee, B. Bhuyan, C. M. Brown, D. Fortin, K. Hamano, R. Kowalewski, I. M. Nugent, J. M. Roney, and R. J. Sobie
University of Victoria, Victoria, British Columbia, Canada V8W 3P6

J. J. Back, P. F. Harrison, T. E. Latham, and G. B. Mohanty
Department of Physics, University of Warwick, Coventry CV4 7AL, United Kingdom

H. R. Band, X. Chen, B. Cheng, S. Dasu, M. Datta, A. M. Eichenbaum, K. T. Flood, M. T. Graham, J. J. Hollar, J. R. Johnson, P. E. Kutter, H. Li, R. Liu, B. Mellado, A. Mihalyi, A. K. Mohapatra, Y. Pan, M. Pierini, R. Prepost, P. Tan, S. L. Wu, and Z. Yu
University of Wisconsin, Madison, Wisconsin 53706, USA

H. Neal
Yale University, New Haven, Connecticut 06511, USA

(Dated: January 1, 2018)

We measure the dependence of $\bar{B}^0 \rightarrow D^{*+} e^- \bar{\nu}_e$ on the decay angles and momentum transfer. The data sample consists of $\sim 86 \times 10^6$ $B\bar{B}$ -pairs accumulated on the $\Upsilon(4S)$ resonance by the BABAR detector at the asymmetric e^+e^- collider PEP-II. We specify the three form factors by two ratios R_1 and R_2 , and by a single parameter ρ^2 characterizing the polynomial representing h_{A_1} , the function which describes the momentum-transfer dependence of the form factor A_1 . We determine R_1 , R_2 , and ρ^2 using an unbinned maximum likelihood fit to the full decay distribution. The results are $R_1 = 1.396 \pm 0.060 \pm 0.035 \pm 0.027$, $R_2 = 0.885 \pm 0.040 \pm 0.022 \pm 0.013$, and $\rho^2 = 1.145 \pm 0.059 \pm 0.030 \pm 0.035$. The stated uncertainties are the statistical from the data, statistical from the size of the Monte Carlo sample and the systematic uncertainty, respectively. In addition, based on this measurement, we give an updated value for the CKM matrix element $|V_{cb}|$.

I. INTRODUCTION

The hadronic weak current of the exclusive semileptonic decay $B \rightarrow D^* \ell \nu$ with a light lepton $\ell = e$ or μ can be described by two axial form factors A_1 and A_2 , and one vector form factor V , which are functions of the B -to- D^* momentum transfer squared, q^2 (and though here we present results only for the $\bar{B}^0 \rightarrow D^{*+} e^- \bar{\nu}_e$ decay, the results are expected to be the same with the electron replaced by a muon, and thus apply to all $\bar{B}^0 \rightarrow D^{*+} \ell^- \bar{\nu}$ decays where ℓ is a light charged lepton). These form factors are usually characterized in terms of their ratio parameters R_1 and R_2 , and a slope parameter ρ^2 . These terms will be defined precisely in Sec. II. First measurements of these three parameters were made by the CLEO collaboration [1]. Improved measurements are important for a significant reduction of the experimental error in the determination of the Cabibbo-Kobayashi-Maskawa (CKM) matrix element $|V_{cb}|$. They also provide for improved determinations of $|V_{ub}|$ from inclusive and exclusive semileptonic $b \rightarrow u \ell \nu$ decays by improving the accuracy with which the dominant $b \rightarrow c \ell \nu$ background to these decays is known.

In heavy-quark effective field theory (HQET) [2, 3], the three form factors are related to each other through heavy quark symmetry (HQS). HQET allows for three free parameters, which must be determined by experiment. Deviations from the HQS relationships can be computed as corrections to the theory. They can also be measured, and the parameterization we adopt is inspired by HQET, but allows for such deviations to be extracted and compared against HQET predictions, as we will see in Sec. X.

The data used in this analysis were recorded by the BABAR detector at the PEP-II storage ring, and correspond to 79 fb^{-1} integrated on the $\Upsilon(4S)$ resonance, yielding 86×10^6 $B\bar{B}$ -pairs. There are $\sim 5 \times 10^6$ $B^0 \rightarrow D^* e \nu$ decays in this sample, of which we have reconstructed 16,386 candidates for the decay $\bar{B}^0 \rightarrow D^{*+} e^- \bar{\nu}_e$ using only the $D^* \rightarrow D^0 \pi^+$ decay of the D^* and the $D^0 \rightarrow K^- \pi^+$ decay of the D^0 (the above also includes reconstruction of the corresponding charge conjugate decay chain, and generally charge conjugation is implied everywhere throughout this document).

We introduce here a novel method of extracting form-

factor parameters from the data. We use an unbinned maximum likelihood method, and introduce approximations that allow us to correct for the efficiency and resolution with the limited Monte Carlo (MC) data sample available. The impact of these approximations on our results is studied in detail.

An important difference from the earlier analysis [1] is that in place of a linear parameterization of the q^2 -dependence of the form factors h_{A_1} , used for their main results, we use a higher-order polynomial motivated by theory. The linear form was assumed in similar analyses (in which only $|V_{cb}|$ and the slope form factor were extracted, but not all three form factors) by ARGUS [4], operating at the $\Upsilon(4S)$, and by ALEPH [5, 6], DELPHI [7], and OPAL [8] at LEP. The need for higher-order terms has been indicated by recent data [9]. Further, this extension is also required by theoretical constraints [10], [11], [12]. The inclusion or exclusion of higher-order terms leads to very different values for the parameter ρ^2 (which is defined explicitly in Eq. (10)), as will be discussed further in Sec. X. In order to compare with previous results, we also report the result of a fit obtained with a linear parameterization.

An outline of the paper is as follows: In Sec. II, we define the observables, form factors, decay amplitudes, and parameters. Sec. III describes the relevant aspects of the detector that are most significant for this analysis. Event reconstruction and selection is described in Sec. IV, the Monte Carlo simulation in Sec. V, and the analysis method in Sec. VI. Sec. VII describes fit results, Sec. VIII the goodness-of-fit method and tests, and Sec. IX the estimation of systematic errors. In Sec. X, we summarize the results and compare them to the previous measurements. Appendix A covers technical details of the pseudo-likelihood systematic error estimation method, and Appendix B gives more detail on the determination of the levels of combinatoric and peaking backgrounds.

II. FORMALISM

This section outlines the formalism and describes the parameterization used for the form factors. More details can be found in Refs. [2, 3].

The lowest order quark-level diagram for the decay $\bar{B}^0 \rightarrow D^{*+} \ell^- \bar{\nu}$ is shown in Fig. 1.

*Also with the Johns Hopkins University, Baltimore, Maryland 21218, USA

†Also at Laboratoire de Physique Corpusculaire, Clermont-Ferrand, France

‡Also with Università di Perugia, Dipartimento di Fisica, Perugia, Italy

§Also with Università della Basilicata, Potenza, Italy

¶Deceased

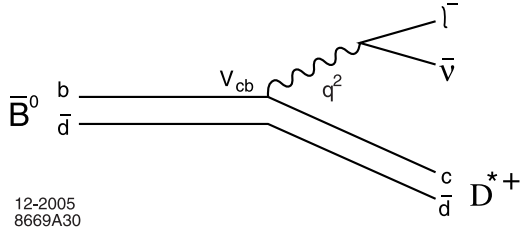


FIG. 1: Quark-level diagram showing the weak interaction vertices in the decay $\bar{B}^0 \rightarrow D^{*+} \ell \bar{\nu}$.

A. Kinematic Variables

A $B \rightarrow D^* \ell \nu$ decay is completely characterized by four variables, three angles and q^2 , the square of the momentum transfer from the B to the D^* meson.

The momentum transfer is linearly related to another Lorentz invariant variable, called w , by

$$w \equiv v_B \cdot v_{D^*} = \frac{p_B \cdot p_{D^*}}{M_B M_{D^*}} = \frac{M_B^2 + M_{D^*}^2 - q^2}{2M_B M_{D^*}}, \quad (1)$$

where M_B and M_{D^*} are the masses of the B and the D^* mesons, p_B and p_{D^*} are their four-momenta, and v_B and v_{D^*} are their four-velocities. In the B rest frame the expression for w reduces to the Lorentz boost to the D^* , $\gamma_{D^*} = E_{D^*}/M_{D^*}$.

The ranges of w and q^2 are restricted by the kinematics of the decay, with $q^2 \approx 0$ corresponding to

$$w_{max} = \frac{M_B^2 + M_{D^*}^2}{2M_B M_{D^*}} \approx 1.504 \quad (2)$$

and $w_{min} = 1$ corresponding to

$$q_{max}^2 = (M_B - M_{D^*})^2 \approx 10.69 (\text{GeV}/c^2)^2. \quad (3)$$

In this analysis we only reconstruct the decay $D^{*+} \rightarrow D^0 \pi^+$, where $D^0 \rightarrow K^- \pi^+$. The angular variables, shown in Fig. 2, are

- θ_ℓ , the angle between the direction of the lepton (i.e., for this analysis, the electron) in the virtual W rest frame, and the direction of the virtual W in the B rest frame
- θ_V , the angle between the direction of the D in the D^* rest frame, and the direction of the D^* in the B rest frame
- χ , the dihedral angle between the plane formed by the $D^* - D$ and the plane formed by the $W - \ell$ system.

B. Four-Dimensional Decay Distribution

The Lorentz structure of the $B \rightarrow D^* \ell \nu$ decay amplitude can be expressed in terms of three helicity amplitudes (H_+ , H_- , and H_0), which correspond to the three

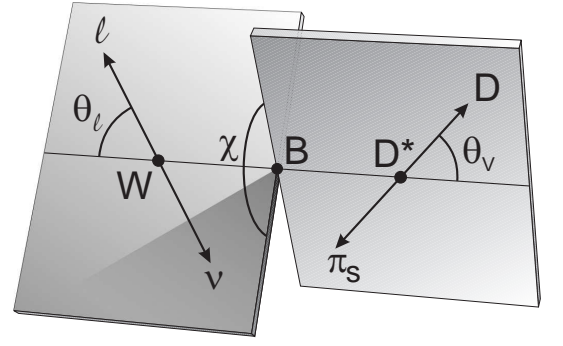


FIG. 2: Kinematics of a $B \rightarrow D^* \ell \nu$ decay, mediated by a weak virtual intermediate vector boson W . This diagram defines the three kinematic variable angles θ_ℓ , θ_V and χ .

polarization states of the D^* (two transverse and one longitudinal). For light leptons these amplitudes are expressed [2, 3] in terms of the three form factors:

$$\begin{aligned} H_+(w) &\equiv -(M_B + M_{D^*})A_1(w) + 2\frac{\wp_{D^*} M_B}{M_B + M_{D^*}}V(w), \\ H_-(w) &\equiv -(M_B + M_{D^*})A_1(w) - 2\frac{\wp_{D^*} M_B}{M_B + M_{D^*}}V(w), \\ H_0(w) &\equiv -\frac{M_B + M_{D^*}}{M_{D^*} \sqrt{q^2}} [A_1(w)(M_{D^*}(wM_B - M_{D^*})) \\ &\quad - \frac{4M_B^2 \wp_{D^*}^2}{(M_B + M_{D^*})^2} A_2(w)], \end{aligned} \quad (4)$$

where $\wp_{D^*} \equiv M_{D^*} \sqrt{w^2 - 1}$ is the magnitude of the momentum of the D^* in the B rest frame (for the τ lepton, which has non-negligible mass compared to the other particles in this process, a fourth helicity amplitude, H_t , would contribute [2]).

The full differential decay rate in terms of the three helicity amplitudes is [2, 3]

$$\begin{aligned} \frac{d\Gamma}{dq^2 d\cos\theta_\ell d\cos\theta_V d\chi} &= \frac{3G_F^2 |V_{cb}|^2 \wp_{D^*}^2 q^2}{8(4\pi)^4 M_B^2} \mathcal{B}_{D^*D} \times \\ & [H_+^2 (1 - \cos\theta_\ell)^2 \sin^2\theta_V + \\ & H_-^2 (1 + \cos\theta_\ell)^2 \sin^2\theta_V + \\ & 4H_0^2 \sin^2\theta_\ell \cos^2\theta_V \\ & - 2H_+ H_- \sin^2\theta_\ell \sin^2\theta_V \cos 2\chi \\ & - 4H_+ H_0 \sin\theta_\ell (1 - \cos\theta_\ell) \sin\theta_V \cos\theta_V \cos\chi \\ & + 4H_- H_0 \sin\theta_\ell (1 + \cos\theta_\ell) \sin\theta_V \cos\theta_V \cos\chi], \end{aligned} \quad (5)$$

where $\mathcal{B}_{D^*D} \equiv BF(D^{*+} \rightarrow D^0 \pi^+) \times BF(D^0 \rightarrow K^- \pi^+)$ and where all three of the H_i are functions of w . The four-dimensional distribution of w , $\cos\theta_\ell$, $\cos\theta_V$, and χ described by Eq.(5) is the physical observable from which we extract the form factors.

In this analysis we only deal with the shape and relative normalization of the form factors, and consequently the overall normalization of the rate is irrelevant.

C. Heavy Quark Symmetry Relations

The functions $R_1(w)$ and $R_2(w)$ are defined in terms of the axial and vector form factors by

$$A_2(w) \equiv \frac{R_2(w)}{R^{*2}} \frac{2}{w+1} A_1(w), \quad (6)$$

and

$$V(w) \equiv \frac{R_1(w)}{R^{*2}} \frac{2}{w+1} A_1(w), \quad (7)$$

where the constant R^* is defined by

$$R^* \equiv \frac{2\sqrt{M_B M_{D^*}}}{(M_B + M_{D^*})}. \quad (8)$$

Perfect HQS implies that $R_1(w) = R_2(w) = 1$, *i.e.*, the form factors A_2 and V are identical for all values of w and differ from A_1 only by a simple kinematic factor. Since HQS is not exact, in general R_1 and R_2 will differ from unity and exhibit some w -dependence as discussed in Sec. II D.

It is conventional to introduce

$$h_{A_1}(w) \equiv \frac{1}{R^*} \frac{2}{w+1} A_1(w), \quad (9)$$

such that in the HQS limit, h_{A_1} is the Isgur-Wise function $\xi(w)$ [13] and $h_{A_1}(1) = \xi(1) = 1$.

The function h_{A_1} can be parameterized in a number of ways. One simple empirical expansion in $w - 1$ is

$$h_{A_1}(w) = h_{A_1}(1) \times (1 - \rho^2(w-1) + \lambda(w-1)^2 + \kappa(w-1)^3 + \dots), \quad (10)$$

We will not fit with this general expansion as there are good theoretical constraints (see Eq. (11)), which relate all the higher-order parameters to the linear ρ^2 parameter. Further, convergence issues arise with attempts to fit a free functional form with so many parameters (see Sec. VII B).

Corrections to HQS modify $h_{A_1}(1)$ and thus lead to deviations from the relation of $h_{A_1}(1) = 1$. In the baseline analysis we use a parameterization of h_{A_1} which conforms to requirements of analyticity. This was first developed and presented by Boyd, Grinstein, and Lebed [11], though the form used here employs a version of this parameterization proposed by Caprini, Lellouch, and Neubert (CLN) [10]

$$h_{A_1}(z) = h_{A_1}(1) \times [1 - 8\rho^2 z + (53\rho^2 - 15)z^2 - (231\rho^2 - 91)z^3], \quad (11)$$

where

$$z \equiv \frac{\sqrt{w+1} - \sqrt{2}}{\sqrt{w+1} + \sqrt{2}}. \quad (12)$$

The maximum value of z over the entire allowed range of w is $z_{max} = 0.04$. In an expansion in $z(w)$ to $\mathcal{O}(w-1)$, ρ^2 is the coefficient of the linear term. In this case, ρ^2 can be referred to simply as the slope $\frac{dh_{A_1}}{dw}$ at $w = 1$. However, in higher-order expansions of $z(w)$, the coefficient of $(w-1)^2$, called the ‘‘curvature,’’ will take on non-zero values, as will coefficients of $(w-1)^3$ and other higher-order terms. Thus, even though only the single parameter ρ^2 is used, the functional form of Eq.(11) implies a non-linear function for $h_{A_1}(w)$.

An alternative parameterization motivated by HQS is

$$h_{A_1}(w) = \left(\frac{2}{w+1}\right)^{2\rho^2}. \quad (13)$$

Le Yaouanc, Oliver and Raynal have demonstrated that this form obeys the bounds on the derivatives they obtain in the HQS limit using a rigorous, general approach based on Bjorken-like sum rules [12].

We do not use this form in our analysis, but note that in the ρ^2 range of interest ($\sim 1 - 1.5$) it agrees with CLN to a few percent. Thus, ρ^2 obtained using this parameterization would be virtually identical to that we obtain using Eq.(11).

D. Form-Factor Ratios

As discussed in Sec. II C, for infinitely massive b and c quarks, HQS predicts $R_1 = R_2 = 1$ exactly. However, these simple relations are broken for finite b and c quark masses, because these ratios are modified by both perturbative (α_s -dependent) and non-perturbative ($\frac{\Lambda_{\text{QCD}}}{m_x}$) corrections, where m_x represents either the b or c quark mass.

Calculating higher-order loop corrections to the form factors yields expansions of the form [14]:

$$R_1(w) = 1 + [\phi_{11}\alpha_s + \phi_{12}\alpha_s^2] + \omega_1 \left(\frac{\Lambda_{\text{QCD}}}{m_x}\right), \quad (14)$$

$$R_2(w) = 1 + [\phi_{21}\alpha_s + \phi_{22}\alpha_s^2] + \omega_2 \left(\frac{\Lambda_{\text{QCD}}}{m_x}\right). \quad (15)$$

The coefficients ϕ_{ij} of the α_s terms are complicated expressions of the D^* boost w which have been calculated perturbatively up to second order, to an estimated accuracy of about one percent (see [14]). Though they are

not explicitly suppressed by a $\frac{1}{m_Q}$ heavy quark mass corrections, they are all functions that approach zero in the $w \rightarrow 1$ HQS limit.

The coefficients ω_i of the $\left(\frac{\Lambda_{\text{QCD}}}{m_x}\right)$ factors are called “subleading Isgur-Wise functions.” Subleading Isgur-Wise function correction terms are evaluated somewhat differently in various models in the HQET framework, resulting in a variety of predictions for $R_1(w)$ and $R_2(w)$.

Perturbative quantum chromodynamics (QCD) and a variety of other theoretical tools have been employed to determine the behavior both at and away from the $w = 1$ endpoint. Close and Wambach used a simple quark model [15] to find

$$R_1(w) = 1.15 - 0.07(w - 1), \quad (16)$$

$$R_2(w) = 0.91 + 0.04(w - 1). \quad (17)$$

Calculations with HQET have produced a variety of results. An early prediction by Neubert was [2]

$$R_1(w) = 1.35 - 0.22(w - 1) + 0.09(w - 1)^2, \quad (18)$$

$$R_2(w) = 0.79 + 0.15(w - 1) - 0.04(w - 1)^2. \quad (19)$$

More recently, CLN [10] used spectral functions, dispersion relations, and HQS to predict

$$R_1(w) = 1.27 - 0.12(w - 1) + 0.05(w - 1)^2, \quad (20)$$

$$R_2(w) = 0.80 + 0.11(w - 1) - 0.06(w - 1)^2. \quad (21)$$

Ligeti and Grinstein [14] using similar HQET calculational tools find

$$R_1(w) = 1.25 - 0.10(w - 1), \quad (22)$$

$$R_2(w) = 0.81 + 0.09(w - 1). \quad (23)$$

It can be seen that in all the predictions the coefficients of the $(w - 1)$ and $(w - 1)^2$ terms are small; this is because R_1 and R_2 are, by construction, ratios that are expected to vary only slightly with w , whereas h_{A_1} is not subject to such a restriction. For the predictions above, R_1 and R_2 vary by 0.07 or less over the full w range. For this reason, for our baseline fit, we follow precedent in treating R_1 and R_2 as constants, independent of w . We will however examine deviations from this baseline fit in Sec. VII.

III. THE BABAR DETECTOR

The BABAR detector is described elsewhere in detail [16]. This analysis uses four of the five subdetectors of BABAR: the silicon vertex tracker, the drift chamber, a Cerenkov-light-based particle identification detector, and the electromagnetic calorimeter. The analysis depends critically on the silicon vertex tracker to reconstruct the low-momentum pions produced by the decay

$D^{*+} \rightarrow D^0\pi^+$, about two-thirds of which do not traverse more than the first quarter of the drift chamber (as is commonly done, we refer to these as “slow” pions, henceforth denoted “ π_s ”).

IV. RECONSTRUCTION AND EVENT SELECTION

We reconstruct the electron track in the drift chamber and silicon tracker and identify it using particle identification (PID) information from dE/dx measured in the drift chamber, photons captured by the Cherenkov-light detector, and energy deposited in the electromagnetic calorimeter. The D^* is reconstructed through its decay to a low momentum pion (π_s) and a D^0 , and the D^0 through its decay to $K\pi$. The hadrons are selected by similar PID information to that used for the electron identification.

We then choose final cuts that select $B \rightarrow D^* e \nu$ decay candidates, and from the four-momenta of the observed particles we determine the kinematic variables w , $\cos\theta_\ell$, $\cos\theta_V$, and χ .

A. Backgrounds and Event Selection

1. Background Categories

We address each distinct source of background with appropriate cuts (which are further described below in Sec. IV A 2):

1. Combinatorial background: events in which the reconstructed D^* candidates that were not originally actual D^* mesons. These events do not contribute to the peak in the $\Delta m = m_{K\pi^+\pi^-} - m_{K\pi}$ distribution. Cutting on Δm provides discrimination against this background.
2. Peaking background, for which the D^* decay has been correctly reconstructed and which contributes to the peak in the Δm distribution. This category is further broken into two main sub-categories:
 - (a) D^{**} background: Events where a true D^* is combined with a electron from the same B^0 or B^- parent, but an extra pion in the decay has been missed. This is primarily feed-down from P-wave D meson decays, but also includes non-resonant $B \rightarrow D^* e \nu X$ decays, where X is $n\pi$ ($n \geq 1$). As shorthand we call this “ D^{**} background” after its dominant component. Note though that the four P-wave D meson states are usually referred to by the shorthand term “ D^{**} modes” in the literature, and thus our redefinition for the purposes of this paper of “ D^{**} background” differs slightly from the standard terminology.

(b) Other events with a true D^* :

- **Fake electron:** Events in which a real D^* is combined with a hadron instead of an electron. This background is minimized by requiring electrons to pass the most stringent electron-identification criteria.
- **Cascades:** Events with a decay chain of the form \bar{B}^0 or $B^- \rightarrow D^*X$, $X \rightarrow eY$ (X is *e.g.*, another D^* or D^0 , Y is anything), so that the observed electron is not primary (*i.e.*, not directly from a B decay). Secondary electrons have a softer momentum spectrum than primary electrons so that a minimum electron momentum cut is effective against this background source.
- **Uncorrelated electron:** Events where a D^* is combined with an electron from the other B . Thus, one side has a \bar{B}^0 or $B^- \rightarrow D^*X$, and the other has B^0 or $B^+ \rightarrow Ye$. A cut on $\cos\theta_{BY}$, the cosine of the angle between the B and the $D^* - e$ combination, is effective against this background.
- **Continuum:** $e^+e^- \rightarrow c\bar{c}$ events for which one c quark forms a D^* while the other hadronizes into a state which decays semileptonically to create an electron ($c\bar{c} \rightarrow D^*eX$). The other continuum backgrounds ($e^+e^- \rightarrow u\bar{u}, d\bar{d}, s\bar{s}$) are negligible and almost none of them pass the final cuts. Cuts on the D^* momentum and event topology are effective at suppressing this background.

2. Event Selection Cuts

For event selection we use the procedure developed for the *BABAR* V_{cb} analysis [9]. The most salient cuts are as follows:

- The momentum of the electron in the center-of-mass (C.M.) frame, which is denoted throughout this paper as “ p_ℓ^* ”, is required to be larger than $1.2 \text{ GeV}/c$. This criterion selects B semileptonic decays and suppresses continuum ($e^+e^- \rightarrow c\bar{c}$) and cascade ($B \rightarrow D \rightarrow e$) backgrounds.
- The slow pion from the D^* decay must have a transverse momentum p_t greater than $50 \text{ MeV}/c$. This rejects the mostly fake tracks found below this cut. The efficiency for finding true pion tracks below $50 \text{ MeV}/c$ is small as the majority of the pions stop before leaving enough hits in the vertex detector to be reconstructed.
- The χ^2 probability of the fit of the D^*e vertex, including the beam-spot constraint, must be greater

than 1%. This suppresses inclusion of particles from the other B , *e.g.*, those tracks in uncorrelated electron background events.

- To further suppress continuum background, we select only candidates with $|\cos\theta_{\text{thrust}}| < 0.85$, where θ_{thrust} is the angle between the thrust axis of the D^*e candidate and the thrust axis of the rest of the event.
- The cosine of the angle θ_{BY} between the direction of the B and the direction of the $D^* - \ell$ system can be computed from the kinematics of the $B^0 \rightarrow D^*\ell\nu$ decay (see Sec. IV B). Candidates with $\cos\theta_{BY}$ between -10 and $+5$ have been used to estimate background. We include only events that have $|\cos\theta_{BY}| \leq 1.2$ in the final sample. The cut is set beyond the physical limits at ± 1 to allow for spillover due to resolution.
- The final selection is based on $\Delta m \equiv m_{K\pi\pi_s} - m_{K\pi}$ (the difference between the reconstructed D^* and D^0 masses). We require $0.143 \leq \Delta m \leq 0.148 \text{ GeV}/c^2$.

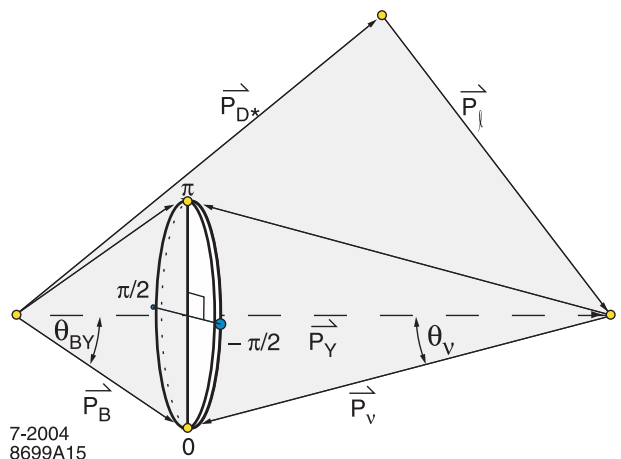


FIG. 3: Reconstructed particle directions and $\cos\theta_{BY}$ in the CM frame. The momentum vectors \vec{P}_{D^*} and \vec{P}_ℓ are measured. Their sum is \vec{P}_Y . The magnitude of the B momentum, $\varphi_B \equiv |\vec{P}_B|$, and the angle θ_{BY} the B makes with \vec{P}_Y are known, but the azimuthal orientation ϕ_{BY} of \vec{P}_B around \vec{P}_Y is not known. The points at $\phi_{BY} = 0, \pi$ are in the $D^* - \ell$ plane.

B. Determination of Kinematic Variable w

Lacking a measurement of the neutrino momentum, we do not have sufficient information to fully reconstruct the kinematic variables w , $\cos\theta_\ell$, $\cos\theta_V$, and χ . However, using energy-momentum conservation and assuming that the missing particle is a massless neutrino, we have

$$0 = m_\nu^2 = M_B^2 + M_Y^2 - 2E_B E_Y + 2\varphi_B \varphi_Y \cos \theta_{BY}, \quad (24)$$

where $p_Y \equiv p_{D^*} + p_\ell$ is the four momentum of the combined D^* and electron, $M_Y^2 = p_Y^2$ is the mass squared and φ_Y is the magnitude of the Y three-momentum. The B meson energy E_B and three-momentum magnitude φ_B are known from the energies of the colliding beam particles, so we can solve for $\cos \theta_{BY}$:

$$\cos \theta_{BY} = -\frac{M_B^2 + M_Y^2 - 2E_B E_Y}{2\varphi_B \varphi_Y}. \quad (25)$$

Thus we can determine the angle between the B and the direction ($\hat{Y} = \vec{p}_Y / \varphi_Y$, where \vec{p}_Y is the three-vector momentum of the Y) of the $D^* - \ell$ system, but we do not know the azimuthal angle ϕ_{BY} . This is illustrated in Fig. 3 where it can be seen that the direction of the B must lie on the cone centered on \hat{Y} with the opening angle θ_{BY} .

For each possible ϕ_{BY} we can compute the kinematic variables w , $\cos \theta_\ell$, $\cos \theta_V$, and χ . Since the angle ϕ_{BY} is not measured, we average over four points: two in the D^* -electron plane corresponding to the azimuthal angles $\phi_{BY} = 0$ and π and two points out of the plane corresponding to the angles $\pm\pi/2$. Further, since $B\bar{B}$ production follows a $\sin^2 \theta_B$ distribution in the angle between the B direction and the beam collision axis in the CM ($\mathcal{I}(4S)$) frame, we weight the kinematic variables evaluated at each point by $\sin^2 \theta_B$.

Fig. 4 illustrates the resolution achieved by this technique. The core widths for each resolution distribution are small compared to the full range of each kinematic variable. The resolution is dominated by the average over the B direction; detector resolution makes a relatively minor contribution. The low-side tail on $\cos \theta_\ell$ can be attributed to final state radiation.

The resolutions of the four kinematic variables are highly correlated. Thus, we rely on Monte Carlo simulation to account for resolution effects.

The distributions of the reconstructed kinematic variables w , $\cos \theta_\ell$, $\cos \theta_V$, and χ from Monte Carlo simulation are displayed in Fig. 5. The shaded region is the distribution of the background as estimated from the Monte Carlo simulation using the method described in Sec. VI below. The background contributions to the distributions are much smaller than the signal contribution (on the order of 10-15%).

V. SIMULATION

This analysis is dependent on Monte Carlo (MC) simulation to model the efficiency and the background distributions. The degree to which the simulation reproduces both the detector response and the underlying physics processes largely determines the systematic errors.

The response of the BABAR detector is modeled using a GEANT4-based simulation. [17]. The simulation has been extensively validated by comparison with large data control samples (such as slow pions from generic $D^* \rightarrow D^0 \pi$ decays for the slow pion helicity studies). Event generation and particle decay are modeled using the package EvtGen [18].

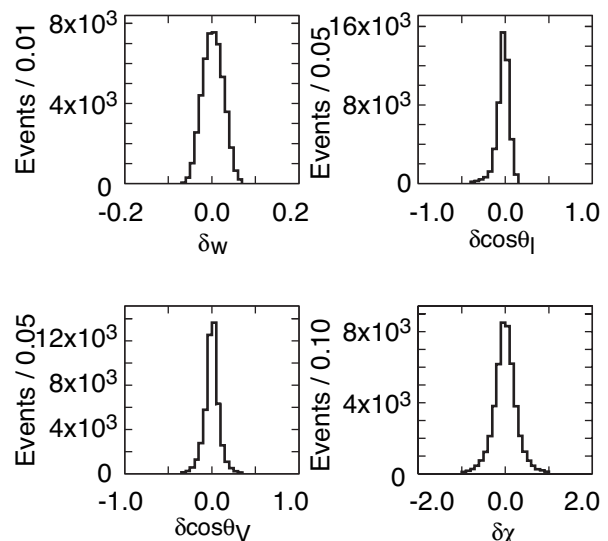
A. Signal

To simulate the signal we use Eq. (5) for the distribution of the decay products. The MC samples are generated with the default parameters $R_1 = 1.180$, $R_2 = 0.720$ and $\rho^2 = 0.920$ [19]. The MC generator uses a simple linear expansion (Eq. (10) taken to order $(w - 1)$), so we must reweight the MC events to model a more complex behavior such as that given by Eq. (11).

B. Detection of Slow Pions

Of particular importance to this analysis is the modeling of the efficiency for detecting low-momentum pions. This task requires detailed simulation work since low momentum pions are lost through the interplay of acceptance, decay-in-flight, and stopping and scattering in the beam pipe and vertex detector.

To test this modeling we examine a large control sample of inclusively produced D^{*+} mesons. Fig. 6 shows the



2-2006
8699A14

FIG. 4: Monte Carlo assessment of the experimental resolution for the variables w , $\cos \theta_\ell$, $\cos \theta_V$, and χ . For each variable the difference between reconstructed and generated values is shown. The resolutions are small compared to the kinematic ranges of the variables as shown in Fig. 5.

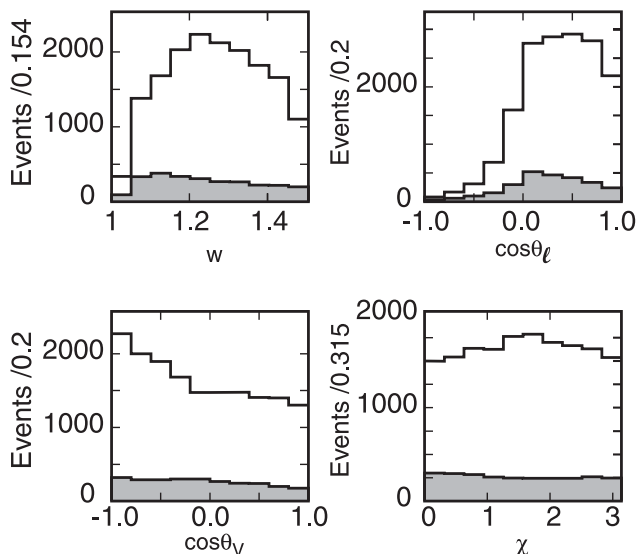
7-2004
8699A1

FIG. 5: One-dimensional projections from Monte Carlo simulation of kinematic variables w , $\cos\theta_\ell$, $\cos\theta_V$, and χ for selected events. The blank region represents signal, and the shaded regions are estimated backgrounds; the histograms are a sum of both the signal and the estimated background beneath them.

distribution of cosine of the helicity angle for the decay $D^{*+} \rightarrow D^0\pi^+$ reconstructed in both the data and the MC sample in bins of D^{*+} center-of-mass momentum. The helicity is defined so that slower pions correspond to backward helicity angle (and is $\cong -\cos\theta_V$).

The MC distributions have been fit to the data using a simple weighting factor of the form

$$f_{\text{corr}} = N (1 + \xi_j \cos\theta_{\pi_s} + \zeta_j \cos^2\theta_{\pi_s}), \quad (26)$$

where the normalization N and the parameters ξ_j and ζ_j have been obtained for each momentum bin j . The three lowest momentum bins are most relevant to $B \rightarrow D^*\ell\nu$ decays. The agreement between the weighted simulation and the data is excellent. Note the weighting factor Eq.(26) is not applied to correct the signal. Rather the weight coefficients obtained by fitting this control sample measure the MC-data differences in each momentum bin.

The linear terms, ξ_j , arise from inadequacies in the simulation of the detector response. The linear terms for the first three bins are small: 0.037 ± 0.160 , -0.023 ± 0.024 and -0.016 ± 0.009 , indicating good agreement between the data and Monte Carlo simulation efficiencies in the complicated arena of slow pion modeling. Note that critical details of the distributions that are unaffected by the weighting scheme (such as the evident thresholds in the low momentum bins) are reproduced correctly by the MC.

The quadratic terms arise mostly from incorrect simulation of the polarization of the D^* -mesons. The values

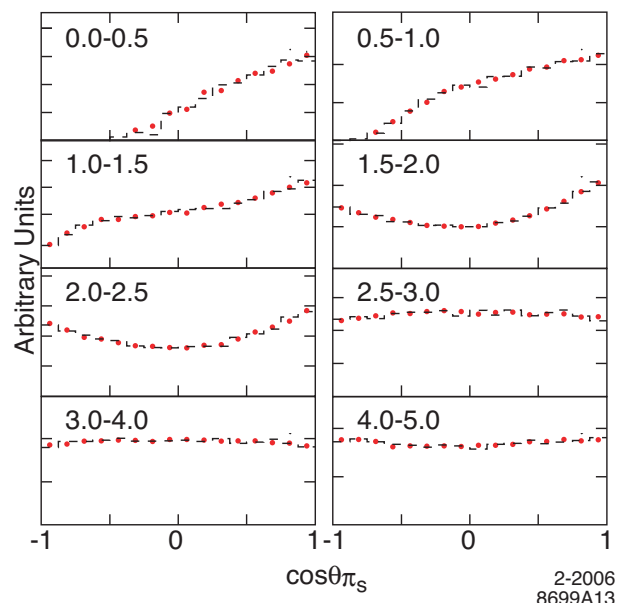
2-2006
8699A13

FIG. 6: Events vs. the cosine of the slow pion angle relative to the line-of-flight of the D^* , shown for bins of CM momentum of the D^* . The momentum ranges for each plot, in GeV/c, are indicated in the upper left-hand corners. Data (points) and MC simulation (histogram) are shown for slow pions from the decay of inclusively produced D^* mesons. The vertical scale is arbitrary, but corresponds to the number of background-subtracted reconstructed D^* candidates in a given bin. Only the differences between data and MC points are relevant for our purposes. The errors are comparable to the dots representing the data. The simulation has been weighted by restricted functions to fit to the data as described in the text.

of ζ are large (~ 0.5 and 0.7) in the momentum bins for $0.5 - 1.0$ GeV/c and $1.0 - 1.5$ GeV/c, where we expect D^* -mesons to be highly polarized products of few-body B -meson decays. These terms do not indicate any problem with detector simulation, and only affect a tiny fraction of the events in our final sample (the fake electron background).

Further, as the MC and data agree well for the linear terms, there is no need to make corrections to account for differences between simulation and data. This is further indicated by the lower right plot of p_{t,π_s} shown in Fig. 12, which indicates excellent agreement between the slow pion transverse momentum distribution after the final fit, but with no linear weighting terms applied to the slow pion momentum.

As the extraction of form factors (especially ρ^2) is highly sensitive to the slow pion simulation we do add a contribution to the systematic error to account for the possible residual differences between the data and the MC simulation. We describe our method for doing this in Sec. IX A 3.

C. Final State Radiation

The program PHOTOS [20] is used to model the effects of final state radiation (FSR). PHOTOS uses quantum electrodynamics (QED) to second order in α_{em} (up to two FSR photons can be produced) and is known to provide a quite accurate simulation of the FSR effects [21].

D. Other Semileptonic Decays

A major source of background is other semileptonic B decays. Only the branching fractions for the decay modes $D\ell\nu$, the signal mode $D^*\ell\nu$, and that for the mode $B \rightarrow D_1\ell\nu$ have been measured [22] (*i.e.*, only one of the four P-wave D meson states). The other branching fractions (including the three other P-wave D states and all non-resonant decays) used in the MC simulation are based on models with large theoretical uncertainties. We use fits to the data to constrain these branching fractions as shown in Sec. IX, to minimize their contribution to the systematic background error.

VI. ANALYSIS METHOD

A. Fitting

Our approach to extracting the form factors is to perform an unbinned maximum likelihood fit to the full four-dimensional distribution function (PDF) specified by Eq. (5). We parameterize the form factors in terms of the parameters R_1 , R_2 and ρ^2 as described in Sec. II. The ρ^2 dependence is specified by Eq. (11). Since theoretical predictions show only a mild dependence of R_1 and R_2 on w (see Eqs. (16-18)), we first perform the fit treating them as constants over the entire range of w . We later show (in Sec. VII) how the results vary when the w -dependencies suggested by the Eqs. (16-18) are imposed.

In addition to assuming its form, we must account for the effects of resolution and efficiency on the measured distribution. We adopt approximations that enable us to carry out the maximum likelihood fit to the form factor parameters efficiently with minimal loss in precision.

1. Resolution-Efficiency Correction Method

To account for the efficiency and resolution effects we adapt the approach first employed in the angular analysis of the decay $B \rightarrow J/\psi K^*$ [23] (for more details of the technique see also [24]). The full PDF (\mathcal{F}) including resolution and efficiency is given in terms of the theoretical PDF (F) of Eq. (5) by

$$\mathcal{F}(\tilde{x}; \mu) = \int dx \varepsilon(x) G(\tilde{x}; x) F(x; \mu), \quad (27)$$

where x represents the true variables (w , $\cos\theta_\ell$, $\cos\theta_V$, and χ), \tilde{x} are the observed values of the variables and μ represents the parameters (R_1 , R_2 and ρ^2) that determine the form factors. The efficiency $\varepsilon(x)$ is the fraction of events with parameters x that are detected and $G(\tilde{x}; x)$ is the probability density that an event with true parameters x is reconstructed with parameters \tilde{x} .

The logarithm of the likelihood L that we need to maximize is given by

$$\begin{aligned} \ln L &= \sum_i \ln \left(\frac{\mathcal{F}(\tilde{x}_i; \mu)}{\mathcal{I}(\mu)} \right) \\ &= \sum_i \ln \mathcal{F}(\tilde{x}_i; \mu) - N_{\text{data}} \times \ln \mathcal{I}(\mu), \end{aligned} \quad (28)$$

where the integral

$$\mathcal{I}(\mu) \equiv \int d\tilde{x} \mathcal{F}(\tilde{x}; \mu) \quad (29)$$

is required to normalize the likelihood in the presence of imperfect acceptance. The sum is over our data sample of N_{data} events.

While the distribution $\mathcal{F}(\tilde{x}, \mu)$ can be simulated by Monte Carlo, it is not practical to use it directly as the function to be varied in the maximum likelihood analysis. Instead, we will introduce a method in which we can use Monte Carlo simulation data without any need to extract a detailed model of the efficiency and resolution function.

We now try the approximation

$$\mathcal{F}(\tilde{x}; \mu) \cong f(\tilde{x}; \mu) \equiv \mathcal{F}(\tilde{x}; \mu_{\text{mc}}) \frac{F(\tilde{x}; \mu)}{F(\tilde{x}; \mu_{\text{mc}})}. \quad (30)$$

where μ_{mc} is the parameter set used for generation of the Monte Carlo sample. If we had used the true values of the parameters μ_t in place of μ_{mc} , then the maximum likelihood method would converge to the true values since by inspection the trial function $f(\tilde{x}; \mu)$ would become the true distribution $\mathcal{F}(\tilde{x}; \mu)$. Of course the true values are not known. The use of μ_{mc} introduces a bias proportional to the difference between the Monte Carlo parameter values and the true parameter values, which can be calculated explicitly in the limit of high statistics.

When the approximation $f(\tilde{x}; \mu)$ of Eq. (30) is substituted into the expression for the log-likelihood Eq. (28), it yields

$$\begin{aligned} \ln L &= \sum_i \ln F(\tilde{x}_i; \mu) - \sum_i \ln F(\tilde{x}_i; \mu_{\text{mc}}) \\ &\quad + \sum_i \ln \mathcal{F}(\tilde{x}_i; \mu_{\text{mc}}) - N_{\text{data}} \ln \hat{\mathcal{I}}(\mu, \mu_{\text{mc}}), \end{aligned} \quad (31)$$

where $\hat{\mathcal{I}}(\mu, \mu_{\text{mc}})$ is the integral of the approximation of Eq.(30).

Since terms that are independent of the fit parameters (constant terms) do not affect the point at which the maximum will be found, all the sums that depend only on μ_{mc} can be dropped (*i.e.*, the central two terms of the total sum). The μ -dependent piece has been factored from these constant terms. We are left with a likelihood function that depends only on the theoretical PDF F and on the integral over the resolution and efficiency functions.

The resolution and efficiency occur only through the normalization integral $\hat{\mathcal{I}}(\mu, \mu_{\text{mc}})$.

Using the technique of Monte Carlo integration to evaluate the integral $\hat{\mathcal{I}}(\mu, \mu_{\text{mc}})$ gives

$$\begin{aligned} \hat{\mathcal{I}}(\mu, \mu_{\text{mc}}) &= \int d\tilde{x} \mathcal{F}(\tilde{x}; \mu_{\text{mc}}) \times \frac{F(\tilde{x}; \mu)}{F(\tilde{x}; \mu_{\text{mc}})} \quad (32) \\ &\approx \frac{1}{N_{\text{gen}}} \sum_i \frac{F(\tilde{x}_i; \mu)}{F(\tilde{x}_i; \mu_{\text{mc}})}. \end{aligned}$$

The MC simulation generates events in proportion to $\mathcal{F}(\tilde{x}; \mu_{\text{mc}})$ so the sum over Monte Carlo events approximates the desired integral. The small error introduced by the Monte Carlo evaluation of the normalization integral is determined in Appendix A.

In Appendix A, we demonstrate that the bias introduced by the use of the approximate form Eq.(30) is given by

$$(\mu - \mu_t)_a = \sum_b (\mu_{\text{mc}} - \mu_t)_b M_{ba} \quad (33)$$

where

$$M_{ba} = J_{bc} E_{ca}, \quad (34)$$

and

$$\begin{aligned} J_{bc} &\equiv \left\langle \frac{\partial \ln \frac{\mathcal{F}}{F}}{\partial \mu_b} \frac{\partial \ln F}{\partial \mu_c} \right\rangle - \left\langle \frac{\partial \ln \frac{\mathcal{F}}{F}}{\partial \mu_b} \right\rangle \left\langle \frac{\partial \ln F}{\partial \mu_c} \right\rangle \\ E_{ac}^{-1} &\equiv \left\langle \frac{\partial \ln F}{\partial \mu_a} \frac{\partial \ln F}{\partial \mu_c} \right\rangle - \left\langle \frac{\partial \ln F}{\partial \mu_a} \right\rangle \left\langle \frac{\partial \ln F}{\partial \mu_c} \right\rangle \quad (35) \end{aligned}$$

and where averages are defined by

$$\langle A \rangle \equiv \frac{\int dx \mathcal{F}(x, \mu_t) A(x)}{\int dx \mathcal{F}(x, \mu_t)}. \quad (36)$$

The bias vanishes if the parameters used in the Monte Carlo coincide with the true values. Moreover, the bias vanishes insofar as the ratio \mathcal{F}/F of the smeared distribution to the unsmeared distribution is independent of the parameters μ . Since \mathcal{F} and F probe nearby regions, the derivative of their ratio will be small, so the coefficient

α in Eq. (34) should be much less than one. Numerical evaluation yields values of ~ 0.15 for R_1 and R_2 and ~ 0.03 for ρ^2 . If $\mu_{\text{mc}} - \mu_t$ is comparable to the error, the residual ‘‘bias’’ should be small, and in practice is found to be so.

To achieve $\mu_{\text{mc}} \sim \mu_t$ we reweight the MC used in the efficiency integral computation to the fitted values of the parameters and iterate until the fit values converge. At this point $\mu_{\text{mc}} = \mu_{\text{fitted}}$ and should deviate from the truth by an amount comparable to the error. In effect the residual deviation acts like a small increase ($\sim 2\%$) in the statistical uncertainty. The iteration method works well and converges quickly, as discussed further in Sec. VII C.

2. Speeding Computation of Normalization Integral Through Moments Factorization

Because the normalization integral $\hat{\mathcal{I}}(\mu, \mu_{\text{mc}})$ depends explicitly on μ it must be recomputed for every iteration of the procedure that maximizes the log-likelihood. To do this by Monte Carlo integration over the full decay phase space would be prohibitively slow.

For the signal distribution, this integration can be avoided. Since the signal PDF can be written in the following form,

$$F(\tilde{x}; \mu) = \sum_{\alpha} A_{\alpha}(\mu) \times \Xi_{\alpha}(x), \quad (37)$$

i.e., as sum over a product of terms depending only on the fit parameters and terms depending only on the kinematic variables, we can define moments M_{α} by

$$M_{\alpha} = \frac{1}{N_{\text{gen}}} \sum_i \frac{\Xi_{\alpha}(\tilde{x}_i)}{F(\tilde{x}_i; \mu_{\text{mc}})}, \quad (38)$$

where the sum is over reconstructed MC events, *i.e.*, the same sum that defines $\hat{\mathcal{I}}(\mu, \mu_{\text{mc}})$ in Eq. (32). This allows us to write $\hat{\mathcal{I}}(\mu, \mu_{\text{mc}})$ as a sum over moments:

$$\hat{\mathcal{I}}(\mu, \mu_{\text{mc}}) = \sum_{\alpha} A_{\alpha}(\mu) \times M_{\alpha}. \quad (39)$$

The moments can be computed once before fitting and then taken as input to the fit. Thus, in the fit, the time-consuming sum over weighted events is replaced with the sum over moments. Taking the expansion of h_{A_1} to order $(w-1)^3$ or z^3 , we have 42 moments to compute and sum.

3. Background Subtraction Through Pseudo-Likelihood

To handle the background, we would ordinarily add a PDF $B(\tilde{x})$ that models the background. The PDF \mathcal{F} would be replaced with

$$f\mathcal{F}(\tilde{x}; \mu) + (1-f)B(\tilde{x}), \quad (40)$$

where f is the signal fraction. However, since we do not have a form for the background distribution before acceptance, we cannot achieve the factorization of the parameter dependence from the efficiency and resolution functions that leads to Eq. (39). To avoid this problem we use the technique of subtracting Monte Carlo events representing the background directly in our likelihood sum rather than adding it to our PDF. We replace our log-likelihood function with the following ‘pseudo-likelihood’ [25]

$$\ln \Lambda = \sum_{i \in \text{data}} \ln F(x_{\text{data}}^{(i)}; \mu) - \sum_{j \in \text{MC}} W_{\text{bkgd}}^{(j)} \ln F(x_{\text{bkgd}}^{(j)}; \mu) - N_{\text{signal}} \ln \mathcal{I}(\mu), \quad (41)$$

where the first sum is over the data and the second is over a Monte Carlo sample representative of the background. The weights $W_{\text{bkgd}}^{(j)}$ account for any difference between the background in the data and in the Monte Carlo. They are computed in the manner indicated by Eqs. (42) and (44) in Sec. VI C below. The coefficient of the normalization integral is $N_{\text{signal}} = N_{\text{data}} - N_{\text{bkgd}}$, where N_{bkgd} is equal to the number of events subtracted, accounting for the weights. It is easy to show that if the Monte Carlo simulation of the background is accurate, the procedure is unbiased. The statistical errors can be computed by a modification of the procedure used for an ordinary log-likelihood analysis.

B. Methodological Error Contributions

The approximations outlined above provide a fast and easily-implemented fitting procedure that uses the MC sample without any need to extract a detailed model of the efficiency and resolution functions. However, these advantages do not come without a cost: we must account for the uncertainty introduced by the resolution-efficiency and pseudo-log-likelihood procedures.

There are three other contributions to the error that are not accounted for in the fit. Two of these are Monte Carlo statistical in nature: the error from the pseudo-log-likelihood subtraction and the error from the Monte Carlo integration used to evaluate $\hat{\mathcal{L}}(\mu, \mu_{\text{mc}})$ in the resolution-efficiency correction procedure. There is also a contribution to the statistical error from the fluctuations in the background that are not accounted for in the fit. The first two can be reduced by increasing the size of the Monte Carlo sample, but the latter error is irreducible and must be included regardless of the size of the Monte Carlo sample.

We have developed procedures for evaluating these three errors. The formulas used are collected in Appendix A.

C. Background Level Estimation

The categorization of backgrounds has been detailed in Sec. IV A. The combinatorial and peaking backgrounds are estimated by fitting the measured $\Delta m = m_{K\pi^+\pi^-} - m_{K\pi}$ and $\cos\theta_{BY}$ distributions in data. The Δm fit determines the combinatorial background. The $\cos\theta_{BY}$ distribution is then fit to a combination of signal, combinatorial background, “ D^{**} ” peaking and other peaking background using the binned likelihood fitting method of Barlow and Beeston [26]. The shape of the $\cos\theta_{BY}$ -distributions are taken from the Monte Carlo simulation. In the fit, only the signal fraction and the portion of the peaking background due to D^{**} and $D^*Xe\nu$ decays are free parameters. The combinatorial fraction is set to the value obtained from the Δm fit and the other components of the peaking background are scaled from the Monte Carlo. See Sec. IV A 1 for more details.

We apply the above procedure first to obtain the overall fractions for the combinatorial (f_{comb}) and the D^{**} ($f_{D^{**}}$) backgrounds. These are obtained by fitting to the full data sample. The fraction of the consolidated remaining peaking backgrounds (f_{otherPk}), detailed in Sec. IV A 1, is obtained by direct scaling from the MC simulation.

The weight needed to subtract the correct amount of each background type is given by

$$W_{\text{type}} = \frac{f_{\text{type}} \times N_{\text{data}}}{N_{\text{type}}}, \quad (42)$$

where $\text{type} = \text{comb}, D^{**}$ or *other* depending on the particular background type being subtracted and N_{type} is the number of Monte Carlo events of that type available.

The determination of f_{comb} and $f_{D^{**}}$ is discussed in more detail in the next two subsections.

1. Determination of Level of Combinatorial Background

The combinatorial background is due to D^* candidates that were not originally actual D^* mesons. It includes candidates where the D is properly reconstructed, but is paired with a random π ; events in which the π_s is in fact from the decay $D^* \rightarrow D\pi_s$, but the D is not properly reconstructed; and candidates which are purely combinatoric (neither the D nor the π_s are correctly reconstructed) – *i.e.*, where any one or more of the three detected particles does not originate from the decay chain $D^* \rightarrow D\pi_s \rightarrow (K\pi)\pi_s$.

To model this background we use the following functional form

$$f(\Delta m) = N \left(1 - \exp\left(\frac{\Delta m - \Delta m_{\text{thr}}}{s}\right)^\kappa \right) \left(\frac{\Delta m}{\Delta m_{\text{thr}}} \right)^\gamma, \quad (43)$$

where below the D^* threshold Δm_{thr} we take $f(\Delta m) = 0$. This is an extension of the commonly used threshold

function [9]. To the single scale parameter s the power κ and the factor $\left(\frac{\Delta m}{\Delta m_{\text{thr}}}\right)^\gamma$ have been added as extra degrees of freedom. This extension allows us to obtain a better fit to the background and allows the fit enough freedom to account for the uncertainty in the background shape. Fixing $\kappa = 1$ and $\gamma = 0$ corresponds to the usual unextended threshold function (further details of the necessity of this extension are given in Appendix B).

The signal distribution is fit by three free Gaussian functions plus a fixed tail of two wide Gaussians. The tail is fixed by fitting pure signal Monte Carlo as described in Appendix B.

The final fit to data is shown in Fig. 7.

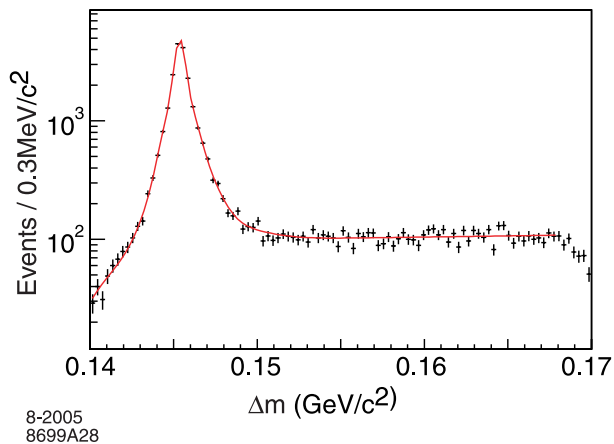


FIG. 7: The fit (solid line) to the Δm distribution for $D^* e\nu$ candidates as described in the text. The distribution is shown logarithmically to emphasize details of the functional fit, but the actual level of background is more clearly seen in the linear data plot shown in Fig. 16.

2. Determination of Level of D^{**} Background

To estimate the peaking background we use a mixture of Monte Carlo predictions and a fit to the $\cos\theta_{BY}$ distribution within the D^* signal window $\Delta m = 0.143 - 0.148 \text{ GeV}/c^2$. We fit the $\cos\theta_{BY}$ distribution for the signal and the background due to decays of the type $B \rightarrow D^{**} X e\nu$ (called the “ D^{**} ” background, as defined in Sec. IV A 1). The shapes of the $\cos\theta_{BY}$ distributions for the signal and the backgrounds are obtained from the Monte Carlo simulation. The backgrounds other than the D^{**} are fixed at values obtained by scaling from the Monte Carlo by the appropriate luminosity ratios. In the case of fake electrons (which are mostly misidentified pions), we also scale using the misidentification probabilities obtained from the data control sample of pions (specifically from the $BABAR \tau^\pm \rightarrow \pi^\pm \pi^+ \pi^- \nu_\tau$ dataset).

Figure 8 shows the results of this fit to the full data sample. The shading indicates the background source or signal. Only two parameters, the signal and the D^{**}

background fractions, are free in the fit. The combinatorial background is input from the Δm fit. The other peaking backgrounds are scaled from the Monte Carlo simulation as described above.

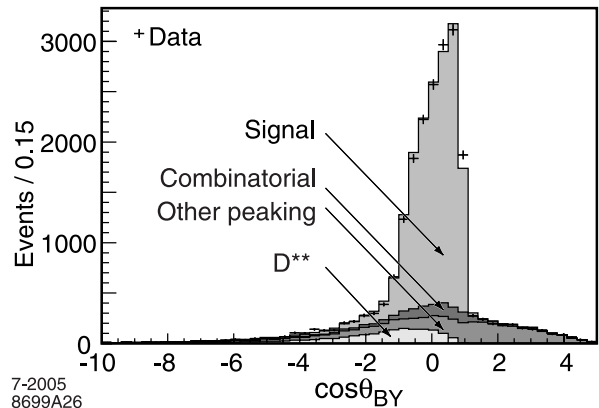


FIG. 8: The $\cos\theta_{BY}$ data distribution and the result of the fit with the estimated signal and background contributions, as described in the text. Shading indicates the various components in the fit.

For input to the form-factor fit we need the background fractions within the $\cos\theta_{BY}$ signal window ($|\cos\theta_{BY}| \leq 1.2$). These are $f_{\text{comb}} = 5.33 \pm 0.26\%$ for the combinatorial, $f_{D^{**}} = 4.85 \pm 0.35\%$ for the D^{**} and $f_{\text{otherPk}} = 7.03 \pm 0.45\%$ for peaking backgrounds other than the D^{**} .

3. Dependence of Background Levels on Kinematic Variables

In addition to obtaining overall background fractions, we perform our Δm - $\cos\theta_{BY}$ fitting procedure in five bins for each of the kinematic variables in the data. This allows extraction of the dependence of combinatorial and D^{**} backgrounds for each kinematic variable. We compare the ratio of fitted background yields in data and MC, and parameterize the difference as a linear function of the kinematic variables. This allows application of a correction term to the weight for each Monte Carlo event of the form:

$$\begin{aligned}
 W_{\text{type}}^{\text{corr}} &= (1 + \alpha_w(w - \langle w \rangle_{\text{type}})) \\
 &\times (1 + \alpha_{\cos\theta_\ell}(\cos\theta_\ell - \langle \cos\theta_\ell \rangle_{\text{type}})) \\
 &\times (1 + \alpha_{\cos\theta_V}(\cos\theta_V - \langle \cos\theta_V \rangle_{\text{type}})) \\
 &\times (1 + \alpha_\chi(\chi - \langle \chi \rangle_{\text{type}})),
 \end{aligned} \tag{44}$$

where the means for each type (which are calculated from the Monte Carlo simulation distributions) are subtracted to keep the normalization independent of the slope.

To extract the dependence of combinatorial background on the kinematic variables, the procedure of fitting four Gaussians for the signal (discussed in Appendix B) and the extended threshold function for the combinatorial background portion is repeated for five bins in each of the four kinematic variables.

To obtain the slopes needed in Eq. (44) we form the ratio of the background estimate in each bin to the number found in that bin in the Monte Carlo simulation and fit it to a straight line. All of the fits are displayed in Fig. 19 Appendix B.

This information is summarized and shown in Fig. 9, and the numerical results for the slopes are given in Table I along with the means, which are needed to do normalization independent weighting, as discussed above after Eq. (44).

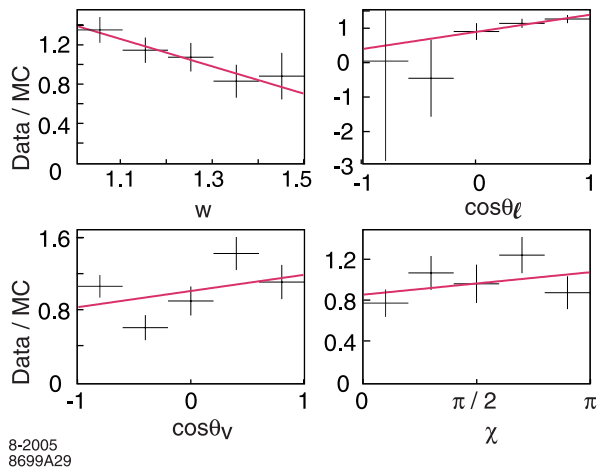


FIG. 9: Ratio of data to Monte Carlo events for combinatorial background for the four kinematic variables w , $\cos\theta_\ell$, $\cos\theta_V$, and χ , obtained from 5-bin fits to data and Monte Carlo in each kinematic variable. The lines are result of linear fits (see text).

TABLE I: The fitted slopes to the distributions shown in Fig. 9 of the ratio of data to Monte Carlo for the combinatorial background in the four kinematic variables w , $\cos\theta_\ell$, $\cos\theta_V$ and χ , and the mean values of the Monte Carlo distributions for these variables.

Variable	Slope	Mean
w	0.51 ± 0.50	1.23
$\cos\theta_\ell$	0.05 ± 0.11	0.31
$\cos\theta_V$	-0.20 ± 0.09	0.00
χ	-0.13 ± 0.06	1.48

As in the combinatorial case, we repeat the extraction of the D^{**} component of the peaking backgrounds in five bins in each of the four kinematic variables. The results of all these $\cos\theta_{BY}$ fits are shown in Fig. 20 in Appendix B. This is summarized in the linear fit for data to Monte Carlo events ratio for the D^{**} background (the compo-

nent free in the fit), which is shown in Fig. 10, with the numerical results in Table II.

The linear fits in Fig. 10 give the slopes used in weighting the backgrounds using Eq. (44).

We use the central slope values to reweight our background subtraction and propagate the errors into the systematic uncertainty by varying the slopes within their errors.

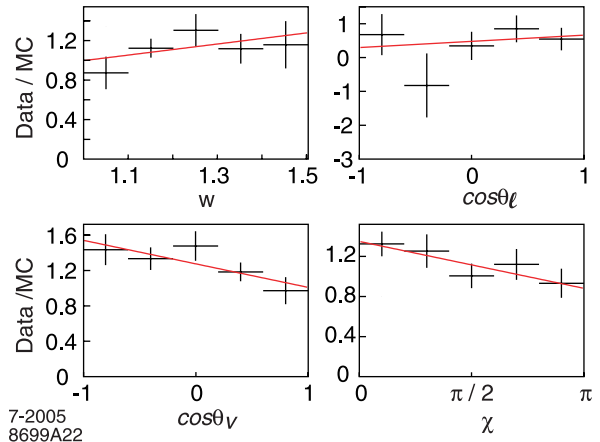


FIG. 10: Ratio of data to Monte Carlo events for D^{**} background for the four kinematic variables w , $\cos\theta_\ell$, $\cos\theta_V$, and χ , obtained from 5-bin fits to data and Monte Carlo in each kinematic variable. The lines are result of linear fits (see text)

TABLE II: The fitted slopes to the D^{**} distributions shown in Fig. 10 of the ratio of data to Monte Carlo for the combinatorial background in the four kinematic variables w , $\cos\theta_\ell$, $\cos\theta_V$ and χ , and the mean values of the Monte Carlo distributions for these variables.

Variable	Slope	Mean
w	-1.35 ± 0.52	1.28
$\cos\theta_\ell$	0.14 ± 0.29	0.35
$\cos\theta_V$	0.18 ± 0.12	-0.11
χ	0.07 ± 0.08	1.53

Further details of the fits and estimates for the background fractions and weights are given in Appendix B.

D. χ Averaging

Few data events arising from true signal will be found at values of the kinematic variables for which the PDF goes to zero. However, there is no such limitation on the number of data events arising from backgrounds that may fall at these points. Because of this, when the logarithm of the PDF is evaluated for these points as part of the background-subtracted computation of the log-likelihood it develops spuriously large (negative) values, driving the fit far astray from the actual minima.

To deal with these spurious zeros we deliberately introduce a small amount of artificial resolution that prevents the PDF from going to zero. This resolution is chosen to be small compared to the natural resolution of our kinematic variable reconstruction (see Fig. 4) and so has little effect on the sensitivity of our measurement. Any small bias introduced is removed by the resolution-efficiency correction method in the same manner as that due to naturally occurring resolution.

We implement this artificial resolution by evaluating the PDF for all data points (including the data, Monte Carlo-selected background, and integration samples, for consistency) at values of the phase space not exactly *at* the given point, but offset from it on both sides in χ by ± 0.1 . The kinematic variable χ is chosen because it is at particular discrete, parameter-dependent values of χ that the theoretical PDF is zero. We then take the values of the PDF for these two offset points and average them. This average is used as the value for the given point in evaluating its contribution to the likelihood.

Testing on Monte Carlo simulation shows χ -averaging does not bias the fit values, nor increase the errors. Varying the value by which we move χ we find that ± 0.1 is small enough to not bias the fit values, and large enough to eliminate the spurious zero problems fully, so we evaluate all fit results with this offset.

VII. RESULTS

A. Free Parameter and Baseline Fits

We perform the baseline fit (see Sec. II C) taking R_1 and R_2 to be independent of w and use the single parameter form factor description of Ref. [10] given in Eq. (11).

We find

$$\begin{aligned} R_1 &= 1.396 \pm 0.060 \pm 0.035, \\ R_2 &= 0.885 \pm 0.040 \pm 0.022, \\ \rho^2 &= 1.145 \pm 0.059 \pm 0.030, \end{aligned} \quad (45)$$

where the first uncertainties given are due to the limitations of the data statistics and the second to limitations of statistics of the Monte Carlo simulations. Systematic uncertainties are discussed in Sec. IX below. The errors are highly correlated. The error matrix for the full statistical error for R_1 , R_2 , and ρ^2 (including Monte Carlo statistical) is:

$$\begin{array}{ccc} 0.00479 & -0.00243 & 0.00277 \\ -0.00243 & 0.00207 & -0.00231 \\ 0.00277 & -0.00231 & 0.00447 \end{array}$$

The correlations are

$$\begin{aligned} \eta_{R_1-R_2} &= -0.77, \\ \eta_{R_1-\rho^2} &= +0.60, \\ \eta_{R_2-\rho^2} &= -0.76. \end{aligned} \quad (46)$$

As we do not yet have enough statistical sensitivity to fit for the w -dependence of $R_1(w)$ and $R_2(w)$, we consider instead the effect of the theoretically predicted dependence on the result. Parameterizing this dependence as follows

$$R_1(w) = R_1 + \alpha_1(w-1) + \beta_1(w-1)^2, \quad (47)$$

$$R_2(w) = R_2 + \alpha_2(w-1) + \beta_2(w-1)^2, \quad (48)$$

and inserting these w -dependent forms into the PDF (with fixed α_i, β_i from the theoretical predictions) and fitting for the constant terms R_1 and R_2 we find the results given in Table III.

These theoretical variations in $R_1(w)$ and $R_2(w)$ yield slightly larger values for R_1 and slightly smaller values for R_2 . However, this is presumably only because they all decrease the mean of $R_1(w)$ and increase the mean of $R_2(w)$ when averaged over the w spectrum.

B. Higher-Order Free Parameter Fits

We performed a study using a large MC sample in order to ascertain whether it was also useful for us to do free fits to h_{A_1} with up to five parameters (see Eq. (10)) for a sample generated with a particular form (the CLN form). To this end, we created a MC sample of a million events generated with the ansatz of Eq. (11) with no acceptance cuts or resolution smearing applied. We then attempted to fit this using four parameters (R_1, R_2 , and coefficients to $\mathcal{O}(w-1)^2$ in h_{A_1}) and five parameters (R_1, R_2 , and coefficients to $\mathcal{O}(w-1)^3$ in h_{A_1}). The fit results for the slope and curvature (for the four parameter fit) and slope, curvature, and cubic term coefficient (for the five parameter fit) were far from the generated values corresponding to the $(w-1)^n$ expansion of the input (Eq. 11).

This problem arises because the fit is attempting to compensate for the missing higher-order terms. As a result the coefficients of $(w-1)$ or $(w-1)^2$ returned by the fit cannot be cleanly interpreted in terms of the theoretical expectations or interpreted in terms of limits such as those given in [12, 27].

Thus, while either the CLN or free polynomial expansion are *a priori* valid, the former is preferred from theoretical constraints, and we see from the above that it is not useful to attempt to fit a sample with a free expansion to a reasonably low expansion order and then interpret the result in terms of CLN coefficients.

Reference	α_1	β_1	α_2	β_2	R_1	R_2	ρ^2
Baseline	0.0	0.0	0.0	0.0	1.40	0.89	1.15
Caprini-Lellouch-Neubert[10]	-0.12	0.05	0.11	-0.06	1.42	0.87	1.12
Ligeti-Grinstein[14]	-0.10	0.0	0.09	0.0	1.42	0.87	1.11
Neubert[2]	-0.22	0.09	0.15	-0.04	1.45	0.86	1.09

TABLE III: Dependence of form-factor parameters on theoretical assumptions about slope (α) and curvature (β) of R_1 and R_2 w -dependence. See Eqs. (47) and (48).

C. Iterative Convergence Studies

We have studied the convergence of the likelihood maximization procedure described in Sec. VI.A. Varying the initial seed values by as much as 50% of the final values still leads to convergence to the same final values within 0.0005 for each parameter within five iterations.

VIII. GOODNESS-OF-FIT

To assess whether the results of the fit reproduce the distribution of the kinematic variables in the data, we use a binned χ^2 method of estimating goodness-of-fit. Chernoff and Lehmann [28] have shown that while a binned χ^2 will in general have a wider than expected distribution when the free parameters are optimized using a likelihood fit, the effect is small for a large number of bins. Therefore we adopt the binned χ^2 as our primary goodness-of-fit test.

Since we do not have an explicit form for the acceptance-corrected PDF (\mathcal{F}) of the four reconstructed variables w , $\cos\theta_\ell$, $\cos\theta_V$ and χ , we reweight the MC sample to construct the distributions expected from our measured parameters. That is, the contribution of the signal to a bin is given by the MC event sum

$$n_{\text{signal}} = \sum_{i \in \text{MC}} W_{\text{signal}}^{(i)}, \quad (49)$$

where

$$W_{\text{signal}}^{(i)} = f_{\text{signal}} \times N_{\text{data}} \times \frac{W_i}{\sum W_i} \quad (50)$$

and in this case $W_i = \frac{F(x_i; \mu)}{F(x_i; \mu_{mc})}$ is the weight needed to modify the distributions from those generated with μ_{mc} ($R_1 = 1.18$, $R_2 = 0.72$, and $\rho^2 = 0.92$), to those obtained from this analysis and $f_{\text{signal}} = 1 - f_{D^{**}} - f_{\text{otherPK}} - f_{\text{comb}}$ is the signal fraction.

For the background we use the same weighting procedure (see Eqs. (42) and (44)) used in the fit. Using these weighting procedures the normalizations of the data and reweighted distributions match by construction.

We consider two types of goodness-of-fit:

- A four-dimensional binned χ^2 based on a total of 1296 bins, that is, $6 \times 6 \times 6 \times 6$ bins, six each for the four kinematic variables

- One-dimensional projected distributions of w , $\cos\theta_\ell$, $\cos\theta_V$, and χ , as well as the distributions of the CM electron momentum (p_ℓ^*) and the transverse momentum (p_t) of the slow pion from the D^* decay.

A. Four-dimensional Binned χ^2

Six bins were chosen for the χ^2 to make sure we have adequate statistics in each bin while still having sensitivity to the shape predicted by Eq. (5) combined with detector and event selection acceptance. The kinematically empty regions shown for Monte Carlo events in Fig. 11a for $w \geq 1.08$ and backward $\cos\theta_\ell$ (due to the electron momentum cut) and in Fig. 11b for small w and forward $\cos\theta_V$ (due to slow pion acceptance) are excluded by simple cuts on minimum $\cos\theta_\ell$ and maximum $\cos\theta_V$ as functions of w , respectively.

The χ^2 is given by

$$\chi^2 = \sum_i \left(\frac{n_i - m_i}{\sigma_{\text{dif}}} \right)^2, \quad (51)$$

where the sum is over the 1296 bins, n_i is the number of data events in bin i , m_i is the weighted number of Monte Carlo events and σ_{dif} is the error on the difference $n_i - m_i$. There is, of course, an error on our estimate of the error σ_{dif} too, that makes the χ^2 contributions from low statistics bins vary widely. Thus, estimating σ_{dif} is critical to obtaining a reasonably behaved χ^2 distribution.

Using a simple Monte Carlo simulation divided into 1296 bins that roughly mimics the number of low statistics bins in our dataset, we can achieve a flat χ^2 probability distribution if we base the error on the best estimate of the number of events in each bin computed using the overall data-to-Monte-Carlo events ratio r_{mc} . That is m_i is given by multiplying the number of MC events n_i^{mc} by r_{mc} .

Specifically, we use $n_i^{\text{best}} = f n_i + (1 - f) m_i$ where $f \equiv r_{\text{mc}} / (1 + r_{\text{mc}})$. The difference error σ_{dif} is obtained by using $\sqrt{n_i^{\text{best}}}$ for the contribution from the data and by scaling the error on m_i by $\sqrt{n_i^{\text{best}} / m_i}$. Thus, we use the hypothesis we are testing (that the weighted Monte Carlo follows the same distribution as the data) to obtain the best possible estimate of σ_{dif} by using the best estimators we can obtain for the number of data events

(n_i^{best}) and for the number of MC events ($n_i^{\text{best}}/r_{\text{mc}}$) to estimate their respective contributions to the error. This procedure reduces the number of bins where the error estimate fluctuates low leading to artificially high χ^2 contributions.

For the baseline fit we find

$$\chi^2 = 1336.66 \quad (52)$$

for 1292 degrees-of-freedom (1296 bins minus three free parameters and one for normalization), which yields a χ^2 probability of 19% indicating the fitted parameters yield a good description of the full four-dimensional distribution of the data (note that we keep two decimal significant digits in χ^2 since every one unit change in corresponds to a full one sigma shift in the fit parameter).

B. One-dimensional Binned Projection Plots

For a more detailed examination of how well we fit the data, we turn to one-dimensional projection plots. Fig. 12 shows the weighted Monte Carlo (histogram) overlaid on the background-subtracted data. The back-

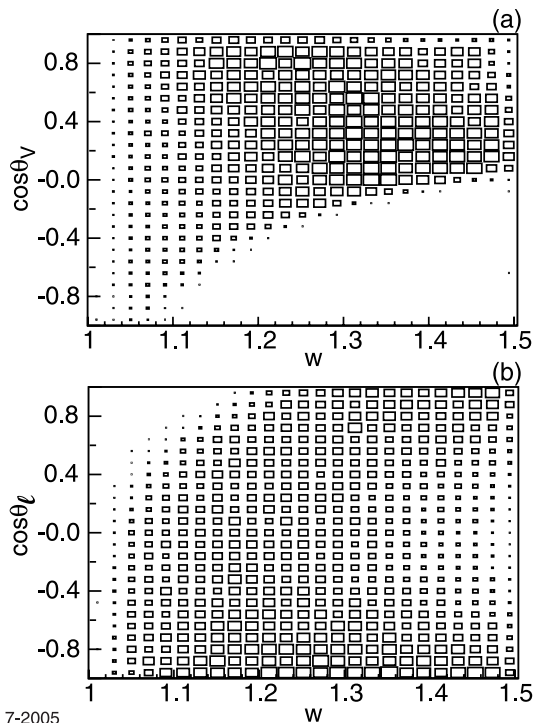


FIG. 11: Plots showing empty regions (due primarily to cuts) in the phase space of the kinematic variables w , $\cos\theta_\ell$, and $\cos\theta_V$ using the Monte Carlo sample: (a) shows $\cos\theta_\ell$ vs. w , where the high w , low $\cos\theta_\ell$ region is removed in the goodness-of-fit calculation; (b) shows $\cos\theta_V$ vs. w , the high $\cos\theta_V$, low w region is removed in the goodness-of-fit calculation.

grounds are subtracted in the one-dimensional analog to the method used in the fit, as detailed in Sec. VI C.

The difference divided by its error (“pull”) is shown below each plot. The agreement is very good. The χ^2 and the corresponding probability for each variable is summarized in Table IV. We take the number of degrees-of-freedom (n_{dof}) to be the number of bins minus one for purposes of estimating the probabilities.

To test our sensitivity to the interference terms in Eq. (5) we make the same kind of comparisons in six bins of the angle χ for the variables $\cos\theta_\ell$ and $\cos\theta_V$. Since the normalization is not fixed in these plots the number of degrees-of-freedom is 20. The $\cos\theta_\ell$ plots are shown in Fig. 13. The $\cos\theta_V$ plots are in Fig. 14. In Table V we collect the χ^2 and its probability for each plot. Again the agreement is excellent indicating that the fit succeeds well in reproducing the details of the distribution.

In these plots we can also see the effect of isolating specific portions of the PDF – *e.g.*, in the very low χ region, $\cos\chi \rightarrow 1$ and we obtain the modulation effect of the $\sin\theta_V \cos\theta_V$ in the fifth term of the PDF, seen in the top left plot in Fig. 14. On the other hand, in the high χ region, $\cos\chi \rightarrow -1$ and this effect flips sign due to the sixth term, as can be clearly seen in the bottom right plot. (These types of effects also occur in Fig. 13 but they are masked by the effect of the p_ℓ^* cut, which suppresses the low $\cos\theta_\ell$ region strongly in that case, so the modulations are more difficult to observe). Much of the information content of our data is encoded in the interference terms, so it is important to ensure that we reproduce their effect accurately.

TABLE IV: χ^2 and χ^2 -probability for kinematic variable projections and electron momentum. The number of bins in these histograms is either 20 or 16.

variable	χ^2/n_{dof}	χ^2 probability
w	22.0/19	28%
$\cos\theta_\ell$	23.0/19	24%
$\cos\theta_V$	31.8/19	3.3%
χ	13.0/19	84%
p_ℓ^*	17.3/19	57%
p_t	9.0/15	88%

IX. SYSTEMATIC STUDIES

The systematic uncertainties on the three parameters R_1 , R_2 and ρ^2 of the baseline fit (see Sec. II C) are summarized in Table VII. The systematic errors are comparable for fits which include variation in w of R_1 and R_2 , such as those shown in Sec. X.

A major source of systematic error arises from the MC simulation, specifically, from the modeling of the detector resolution and efficiency. We are particularly concerned

TABLE V: χ^2 and χ^2 -probability for $\cos\theta_\ell$ and $\cos\theta_V$ overlay plots in six bins of the kinematic variable χ . These values correspond to the numerical evaluation of one-dimensional χ^2 of Figs. 13 and 14.

variable	χ cut	χ^2/n_{dof}	χ^2 probability
$\cos\theta_\ell$	$0 \leq \chi \leq \frac{\pi}{6}$	18.4/20	56%
$\cos\theta_\ell$	$\frac{\pi}{6} \leq \chi \leq \frac{2\pi}{6}$	19.3/20	50%
$\cos\theta_\ell$	$\frac{2\pi}{6} \leq \chi \leq \frac{3\pi}{6}$	29.6/20	7.7%
$\cos\theta_\ell$	$\frac{3\pi}{6} \leq \chi \leq \frac{4\pi}{6}$	17.9/20	59%
$\cos\theta_\ell$	$\frac{4\pi}{6} \leq \chi \leq \frac{5\pi}{6}$	23.9/20	25%
$\cos\theta_\ell$	$\frac{5\pi}{6} \leq \chi \leq \pi$	12.4/20	90%
$\cos\theta_V$	$0 \leq \chi \leq \frac{\pi}{6}$	19.5/20	49%
$\cos\theta_V$	$\frac{\pi}{6} \leq \chi \leq \frac{2\pi}{6}$	26.7/20	14%
$\cos\theta_V$	$\frac{2\pi}{6} \leq \chi \leq \frac{3\pi}{6}$	10.8/20	95%
$\cos\theta_V$	$\frac{3\pi}{6} \leq \chi \leq \frac{4\pi}{6}$	20.1/20	45%
$\cos\theta_V$	$\frac{4\pi}{6} \leq \chi \leq \frac{5\pi}{6}$	27.4/20	12%
$\cos\theta_V$	$\frac{5\pi}{6} \leq \chi \leq \pi$	25.3/20	19%

with the efficiency for reconstructing the low-momentum charged pion from D^{*+} decays.

Further, how well the background event generation is modeled, *e.g.* how close the branching fractions in the event generator are to measured ones, affects the distribution of background we subtract. The kinematic-variable dependence of the backgrounds, however, is not taken from the Monte Carlo but is measured in the data under the assumption that the difference between the Monte Carlo and the data can be represented by a linear kinematic-variable dependence. The uncertainty in this measurement also contributes to the systematic errors. We are also able to check our background estimates using the goodness-of-fit as shown in Section VIII.

Our systematic errors fall broadly into two categories:

- A: Detector simulation, *i.e.*, the accuracy with which the Monte Carlo reproduces the resolution and efficiency of the detector. We are most sensitive to how well it models the complex process of detecting and measuring low-momentum pions.
- B: Simulation of B decays and background, *i.e.*, the accuracy with which our event generation models the signal and background distributions and how well we correct for differences between data and Monte Carlo.

A. Detector Simulation

Extensive studies of the simulation of the detector response, including careful examination of track reconstruction and particle identification efficiencies, have been performed using selected data control samples. Adjustments for known simulation deficiencies are used in investigating and evaluating the systematic errors. Form-factor measurements are insensitive to overall normaliza-

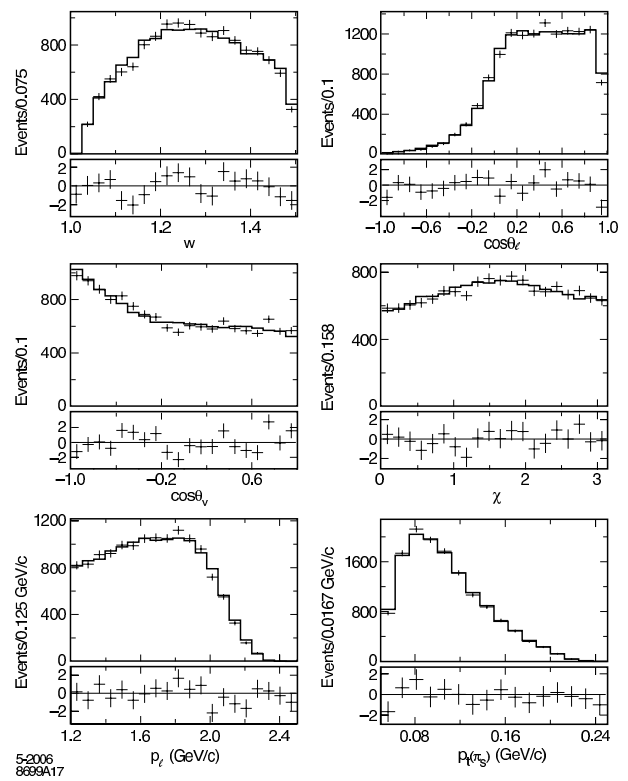


FIG. 12: Background-subtracted data (points) overlaid on Monte Carlo (histograms) for all four kinematic variable distributions and for the electron momentum (p_e^*) and transverse momentum (p_t) of the slow pion for our best fit. In the bottom panel of each figure is shown the pull (difference over error) plot. The red line in the pull plot is not a fit, but is the line at zero shown for comparison (similarly for all following pull plots).

tion errors. Thus differences in the efficiencies that are independent of the fit variables do not affect the results, but MC/data differences that vary as a function of these variables are of concern.

To assess the uncertainties due to differences in shape rather than normalization (Sec. IX A 2–Sec. IX B 1), we vary the efficiency corrections, reweight the Monte Carlo samples with these modified corrections, and rerun the fit to the kinematic variable data. Finally, we take the difference between the results of these fits and those obtained with the nominal Monte Carlo simulation as an estimate of the systematic error on the parameters. This procedure is repeated for each source of detector-based systematic uncertainty. The individual uncertainties are added in quadrature to obtain the total systematic error.

1. Charged Particle Identification (PID)

Using data and Monte Carlo simulated control samples we have studied the difference in particle identification efficiency ε_{pid} between data and Monte Carlo. We calculate

a correction factor, $\varepsilon_{pid}^{(data)}/\varepsilon_{pid}^{(mc)}$, as a function of momentum. For electrons the correction factors vary from 0.991 to 1.008 over the momentum range from 1.2 GeV/c to 2.5 GeV/c. We assess the impact of the uncertainty in these corrections by approximating their momentum dependence by linear functions and varying the size of the small slope of these functions by its one-sigma uncertainty. The observed deviations from the default fit are $\Delta R_1 = 0.0064$, $\Delta R_2 = 0.0052$ and $\Delta \rho^2 = -0.0016$ for the increased slope and -0.0032 , -0.0031 , $+0.0009$ for the decreased slope. We take half of the difference as the systematic error from this source. Since the momentum dependence is not a monotonic function, this procedure slightly overestimates the uncertainty.

For kaon identification we employ the same procedure. The observed variations are significantly smaller.

The probability of misidentifying the charged hadrons π^\pm , K^\pm , p^\pm , as electrons is small, less than 0.2% in the

momentum range 1.2 – 2.5 GeV/c. Since a variation of the peaking background by 9% results in a very modest change in the fit results, and since the fraction of this background originating from hadrons misidentified as electrons is small, we conclude that the uncertainty in the hadron misidentification rate is negligible.

The misidentification rate of pions as kaons as a function of pion momentum ranges from a few tenths of a percent to almost 5%. However, pion misidentification is well simulated by the Monte Carlo and thus should have little impact on the fit results. Furthermore, the main consequence of pion misidentification is to increase the combinatorial background. Since we estimate the combinatorial background from a fit to the measured Δm distribution, we are not dependent on the Monte Carlo to assess the size of this background. We conclude that the uncertainty in the pion misidentification rate has little impact on the fit results.

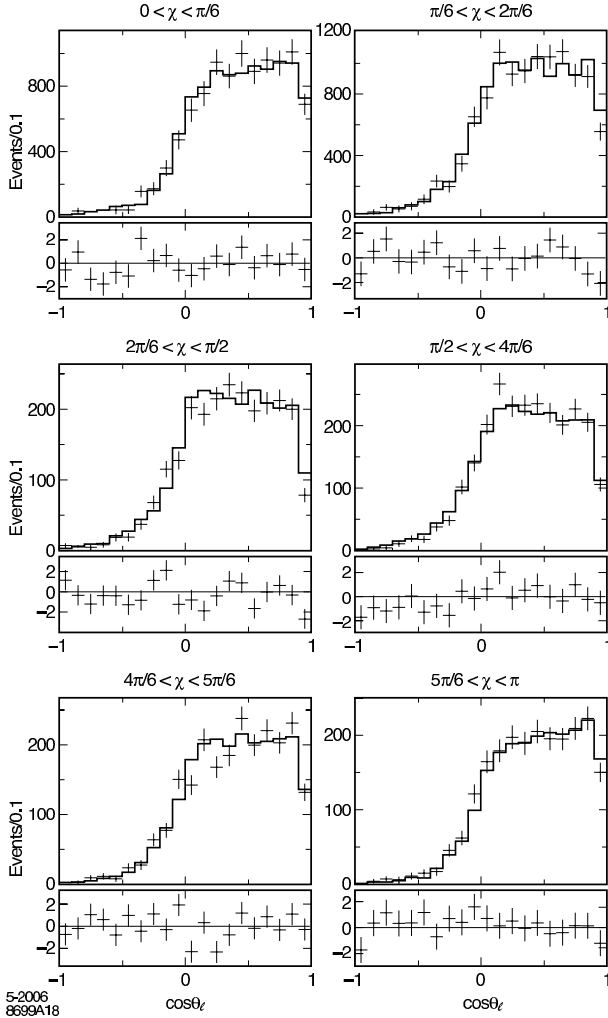


FIG. 13: Background-subtracted data (points) overlaid on Monte Carlo (histograms) and pull plots for $\cos\theta_e$ for six χ cuts.

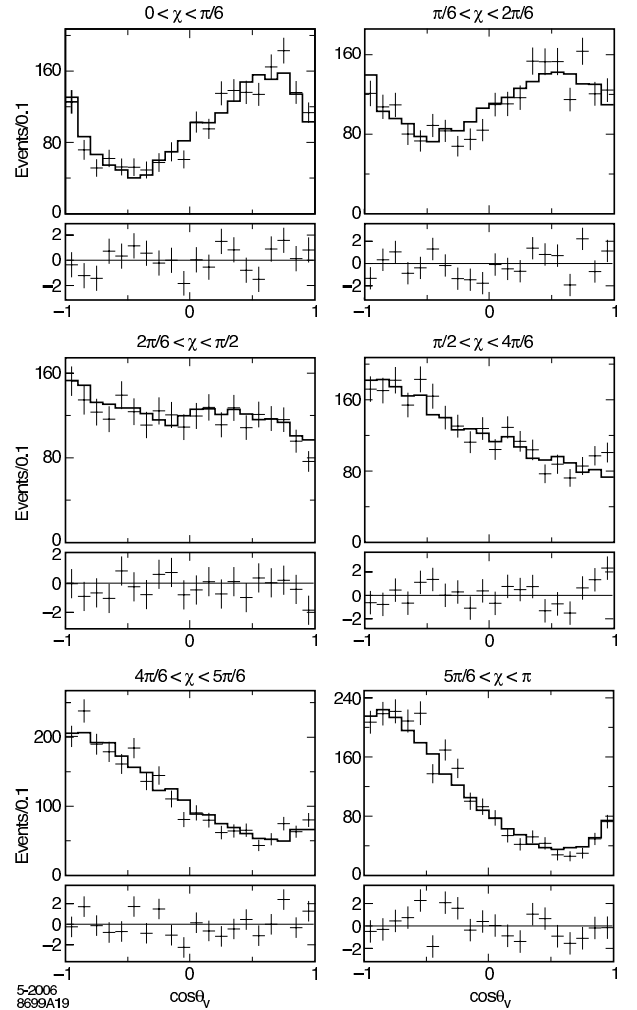


FIG. 14: Background-subtracted data (points) overlaid on Monte Carlo (histograms) and pull plots for $\cos\theta_V$ for six χ bins. These plots illustrate our sensitivity to interference effects.

2. Charged Particle Tracking

The difference between data and Monte Carlo for the tracking efficiency for electrons, charged kaons and pions decreases roughly linearly as a function of momentum. Analogously to the method described for the PID error of Sec. IX A 1, we vary this linear dependence on the particle momentum in the Monte Carlo simulation and take the small deviation as the error from this source. It is a small contribution to the total systematic error.

3. Slow Pion Reconstruction

The efficiency for reconstructing the low-momentum charged pion (π_s) from the decay $D^{*+} \rightarrow D^0 \pi_s$ is a major source of systematic error. Because of the small energy release in D^* decays, this pion is emitted in approximately the same direction as the parent D^* and its momentum in reconstructed events varies from approximately 50 to 400 MeV/ c in the laboratory frame, peaking at ~ 100 MeV/ c , and with a long tail extending out to 400 MeV/ c . Since $w = E_{D^*}/m_{D^*}$ in the B rest frame, the π_s momentum is correlated with w and thus its momentum-dependent efficiency impacts especially the measurement of ρ^2 .

The uncertainty due to the low-momentum tracking efficiency is evaluated differently from other tracking errors because such low-momentum tracks do not traverse the whole drift chamber. Their detection and measurement depends primarily on the silicon vertex tracker. To study this efficiency as a function of p_{π_s} we use a large sample of $D^{*+} \rightarrow D^0 \pi_s^+$ decays selected from all events and measure the distributions of the helicity angle of π_s^+ (θ_{π_s}) in the D^{*+} rest frame as a function of the D^{*+} momentum.

We parameterize the π_s efficiency as function of its momentum using the form

$$\varepsilon(p_{\pi_s}) = \varepsilon_{\max} \left(1 - \frac{1}{1 + \beta(p_{\pi_s} - p_0)} \right) \quad (53)$$

with p_0 being the threshold momentum and β controlling the rapidity with which the efficiency rises above threshold. For $p_{\pi_s} < p_0$ we set ε to zero. We fit the data and Monte Carlo helicity angle distributions for β , p_0 and the coefficient of the $\cos^2 \theta_{\pi_s}$ term (allowed because the D^* is in general polarized to varying degrees in each momentum bin, see Sec. VB) to obtain efficiency functions for the data and the Monte Carlo. The helicity method only determines the relative momentum dependence of the efficiency. The absolute dependency is not relevant for this analysis.

To assess the systematic uncertainty due to the π_s efficiency ($\varepsilon(p_{\pi_s})$) we weight the Monte Carlo simulation by the ratio of the data function to the Monte Carlo function and assign the observed shifts in the fitted values for R_1 , R_2 and ρ^2 as systematic errors. As expected, ρ^2

is the most sensitive ($\Delta\rho^2 = 0.018$) to $\varepsilon(p_{\pi_s})$ since, of all the kinematic variables, $\varepsilon(p_{\pi_s})$ most strongly affects the shape of the w -distribution, which is the kinematic variable that has the strongest impact on the extracted ρ^2 value.

B. Event Simulation

1. Final State Radiation

Final state radiation, primarily from electrons in the decay chain, lowers the momenta and to a lesser degree changes the angles of detected particles. Though a physics effect, final-state radiation acts much like a resolution – it smears the kinematic variables. We simulate the emission spectrum of radiative photons using PHOTOS [20], so the resolution-efficiency correction procedure properly corrects for final-state radiation to the extent that PHOTOS models it correctly.

To test the sensitivity to uncertainty in the simulation of final-state radiation we evaluate the shifts in the fitted values of R_1 , R_2 and ρ^2 between fits done with and without final-state radiation corrections. We assume an uncertainty of 30% in the simulated photon emission and thus take $\sim 1/3$ of the observed shifts (final-state radiation on vs. final-state radiation off) of 0.0129, 0.0067 and 0.0039 as an estimate of the systematic uncertainty.

2. Peaking Background Mixture Uncertainty

The modeling of the peaking background depends on the knowledge of the branching fractions for the mixture of semileptonic B decay modes that make up this background. These branching ratios and the form factors for these modes are not very well measured. To estimate the uncertainty associated with these branching fractions, we use a one-sigma variation of the procedure discussed in Section VI C, *viz.*: we first fit the $\cos\theta_{BY}$ distributions with a sum of functions where the signal fraction and the contribution due to the D^{**} background are allowed to float. This fit is done in five equal-sized bins for each kinematic variable, over the full kinematically allowed range of the variable, in both data and Monte Carlo. We then take data-to-Monte Carlo ratios of the fit results per bin (shown in Fig.(10)), which we then fit to a linear function of the kinematic variables. While for the central value we use this function to weight the D^{**} background itself before it is subtracted from the data, for the error we vary the weighting function up and down by its one-sigma slope uncertainty as shown in Table II. The difference of the original fit minus the result of this fit gives us an estimate of the error due to the uncertainty in the shape of the D^{**} background for each kinematic variable. We add the uncertainties for each kinematic variable in quadrature to give us the total error due to this source.

Another technique of estimating the D^{**} background error is to vary the branching fractions of the P-wave D meson and non-resonant mode components while keeping the overall peaking background fixed. The results of using this technique come out to be of a similar scale to using the above method, which relies on fits to data. Using both techniques would double-count the error, so we rely on the data-fit technique alone to estimate the error from this source.

3. Combinatorial Background Shape Uncertainty

A procedure similar to that employed for the peaking background shape is used to estimate the impact of the uncertainty on the shape of the combinatorial background, except in this case we work with the Δm fits rather than the $\cos\theta_{BY}$ fits. As before, we do this fit in five equal-sized bins for each kinematic variable over the full kinematically allowed range of the variable, in both data and Monte Carlo. We then take data-to-Monte Carlo ratios of the fit results per bin, and find the results shown in Fig.(9), which we then can approximate with linear fits. We use these fit results with their associated one-sigma slope uncertainties shown in Table I to weight the combinatorial background fraction up and down and fit to the data minus this reweighted distribution. The difference from the original fits gives us an estimate of the error due to the shape of combinatorial background uncertainty for each kinematic variable. Adding the uncertainties for each kinematic variable in quadrature gives us the total error from this source.

4. Background Check with Goodness-of-Fit

The quality of the fit as measured by the binned χ^2 (see Sec. VIII) is sensitive to the background fraction assumed. Thus, we can use χ^2 to check our estimate of the backgrounds. Figure 15 shows plots of χ^2 versus the fractions of the combinatorial, D^{**} , and other peaking backgrounds. These scans yield estimates of the background fractions (in percent) of

$$\begin{aligned} f_{\text{comb}} &= 5.4 \pm 1.3, \\ f_{D^{**}} &= 6.1 \pm 1.2, \\ f_{\text{otherPk}} &= 6.4 \pm 0.9, \end{aligned} \quad (54)$$

which are in good agreement with the values of 5.33%, 4.85% and 7.03% obtained from the Δm and $\cos\theta_{BY}$ fits in section VIC.

The good agreement indicates not only that the sizes of these backgrounds are well-estimated, but that the shape in the four-dimensional kinematic-variable phase-space given by the Monte Carlo agrees well with their shape in the data.

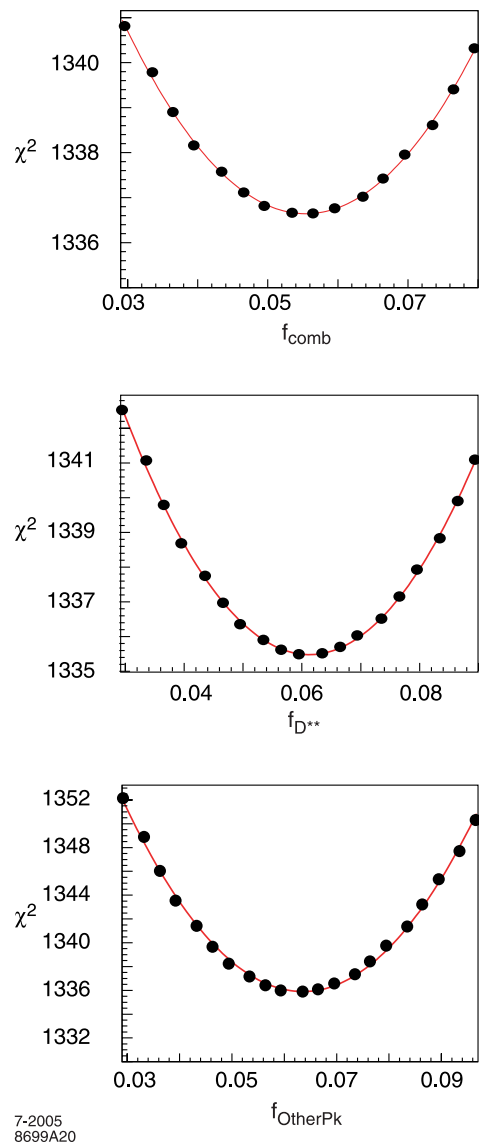


FIG. 15: χ^2 of fit vs. fractions of combinatorial (f_{comb}), D^{**} ($f_{D^{**}}$) and other peaking backgrounds (f_{otherPk}). From this we see that our method of ascertaining the goodness-of-fit is independently indicating that the values we obtained for these fractions from the $\cos\theta_{BY}$ and Δm fits were correct.

5. Total Peaking and Combinatorial Background Fractions

Another source of error is the uncertainty in the normalization of the peaking and combinatorial background fractions. To estimate this error we vary the fractions f_{comb} , $f_{D^{**}}$ and f_{otherPk} by their uncertainties and assess the impact on the fit parameters. The uncertainties for the combinatorial and D^{**} fractions are taken from the Δm and $\cos\theta_{BY}$ fits. However, since f_{otherPk} is input to these fits by scaling the Monte Carlo distribution, we take its uncertainty instead from the goodness-of-fit scan of the previous section. In varying f_{otherPk} we keep

the total peaking $f_{\text{peaking}} = f_{D^{**}} + f_{\text{otherPk}}$ fixed, since this behavior is observed when f_{otherPk} is varied in the $\cos\theta_{BY}$ fit.

6. MC/Data Sideband Comparison

The distributions of the kinematic variables for Monte Carlo and data agree well in the Δm sideband region used to estimate the combinatorial background. But since the combinatorial background comprises about a third of the total background under the peak, the small differences in the shapes of the distributions could introduce an error in the background subtraction process. To estimate the impact of this effect, we first take the data-to-Monte Carlo ratios in the sideband region and then fit these ratios with polynomials.

We next use these functions one at a time to multiply the combinatorial background from Monte Carlo before it is subtracted from the data to prepare the sample for fitting. We then carry through the fits and take the differences in the form factors we obtain from these with the form factors we obtained from the fits with the unaltered background. This procedure yields the results shown in Table VI.

The differences are small. The largest is from using the function for w , from which we find $\Delta\rho^2 \sim 0.006$. Since in the end we take the w -dependence of the combinatorial background from the data and the deviations due to weighting the angular distributions are small, we add nothing to the systematic uncertainty from this check.

TABLE VI: Changes in the fitted parameters for reweighting of the Monte Carlo combinatorial background distributions in the four kinematic variables.

Rewighted distributions	R_1	R_2	ρ^2
w distribution	-0.002	0.0	0.006
$\cos\theta_\ell$ distribution	0.001	-0.002	-0.001
$\cos\theta_V$ distribution	0.002	-0.003	0.001
χ distribution	0.004	-0.002	0.001

C. Summary of Systematic Errors

The systematic errors are summarized in Table VII. The largest contributions to the systematic errors of R_1 and R_2 arise from the uncertainties in background composition, and in the normalization of non- D^{**} peaking backgrounds. On the other hand, the largest contributions to the systematic error of ρ^2 arise from the uncertainties in the kinematic variable-dependence of the backgrounds, in the slow pion tracking efficiency and also in the normalization of non- D^{**} peaking backgrounds.

While the total error remains statistics-dominated, this result is only about a factor of two above the systematic limit. An improved understanding of the systematics would be needed if we were to extend this analysis to other D decay modes and a larger data set.

TABLE VII: Summary of the estimated systematic errors for the baseline fit.

Error source	σ_{R_1}	σ_{R_2}	σ_{ρ^2}
Charged particle track efficiency	0.005	0.004	0.003
Slow pion track efficiency	0.003	0.000	0.018
PID misID (electron, kaon)	0.006	0.004	0.003
D^{**} background normalization	0.003	0.002	0.005
Other peaking backgrounds normalization	0.021	0.006	0.015
Combinatorial background normalization	0.002	0.001	0.003
Bkgd composition (branching fractions)	0.016	0.008	0.005
Kinematic Variable-dependence of bkgd	0.001	0.001	0.028
Final state radiation	0.005	0.002	0.002
Total Systematic	0.027	0.013	0.035

X. SUMMARY AND DISCUSSION

Based on a sample of 16,386 $B^0 \rightarrow D^{*-} e^+ \nu_e$ events, we have measured the form factors A_1 , V and A_2 in terms of the HQET-inspired parameters R_1 , R_2 and ρ^2 . The baseline result, using the CLN parameterization of $h_{A_1}(w)$ (see Sec. II C) is obtained neglecting any possible w -dependence of $R_1(w)$ and $R_2(w)$, and including all errors is

$$\begin{aligned}
 R_1 &= 1.396 \pm 0.060 \pm 0.035 \pm 0.027, \\
 R_2 &= 0.885 \pm 0.040 \pm 0.022 \pm 0.013, \\
 \rho^2 &= 1.145 \pm 0.059 \pm 0.030 \pm 0.035,
 \end{aligned}
 \tag{55}$$

where the first error is statistical, the second Monte Carlo statistical, and the third systematic.

Note that the CLEO result discussed in Sec. I was obtained using the expansion in $(w-1)$ (see Eq. (10)) to linear order. When analyzed in this manner, the current dataset yields $R_1 = 1.40 \pm 0.06$, $R_2 = 0.87 \pm 0.04$, and $\rho^2 = 0.79 \pm 0.06$. CLEO also obtained ρ^2 using the form (see Eq.(13)) suggested by reference [12] that is very close numerically to the CLN parameterization we use. In this case they obtained $\rho^2 = 1.42 \pm 0.32$ which is consistent with our result.

The values of ρ^2 obtained are very different using the linear parameterization, as mentioned in Sec. I. This is because the linear fit significantly underestimates the slope as it attempts to accommodate the higher-order terms (*i.e.*, at $w=1$, the absolute value of the slope is larger assuming a curve for the fit vs. a line).

The χ^2 of this linear fit is 1337.98 which is 1.32 units of χ^2 worse than the baseline fit using the expansion of Eq. (11) (see Eq.(52)). Thus while the baseline fit is slightly better than the linear, both are acceptable.

The sensitivity needed to independently establish the w -dependence of $R_1(w)$ and $R_2(w)$ is not yet available, but theoretical predictions may be used to make comparisons. If we compare the predictions of CLN [10] for $R_1(w)$ and $R_2(w)$ (see Table III) to the baseline result, the shifts are found to be $\Delta R_1 = 1.42 - 1.27 = 0.15$ ($\approx 2.0\sigma$ apart) and $\Delta R_2 = 0.87 - 0.80 = 0.07$ ($\approx 1.5\sigma$ apart). For Ligeti and Grinstein [14] the numbers are $\Delta R_1 = 1.42 - 1.25 = 0.17$ (2.3σ) and $\Delta R_2 = 0.87 - 0.81 = 0.06$ ($\approx 1.3\sigma$). The older prediction of Neubert [2] is closer with ΔR_1 giving $\approx 0.6\sigma$. If the theoretical error on R_1 is ~ 0.03 as estimated by Ligeti [29] then there is a mild indication of disagreement. Higher statistics will be needed to resolve or confirm the possible discrepancy.

These results allow a five-fold reduction in the largest source of systematic error in V_{cb} measurements based on $B \rightarrow D^* \ell \nu$ decays to be made. Using the measurements of R_1 and R_2 presented in this paper, we update the result from the 2004 BABAR paper[9] to find

$$|V_{cb}| = 37.6 \pm 0.3(stat) \pm 1.3(syst) \begin{matrix} +1.5 \\ -1.3 \end{matrix} (theory) \times 10^{-3}.$$

where small correlations between the present analysis and that of Ref. [9] have been ignored. The error due to the uncertainties in R_1 and R_2 is reduced from $\begin{matrix} +2.9\% \\ -2.6\% \end{matrix}$ to $\pm 0.5\%$. The overall systematic error drops from ± 1.7 to ± 1.3 . The other systematic errors remain the same as published in Ref. [9].

A considerable improvement was also obtained in measurements of the lepton endpoint spectrum in $b \rightarrow u \ell \nu$ decays. Compared to usage of the old CLEO $B \rightarrow D^*$ form-factor measurements, usage of these newer form factors allowed the systematic error on the inclusive $B \rightarrow X_u \ell \nu$ branching fraction for decays with a lepton in the momentum range $2.0 - 2.6$ GeV/ c to be reduced from 6.7% to 2.4%. In the higher momentum range $2.3 - 2.6$ GeV/ c the improvement was from 2.8% to 1.3%. This enabled a significant improvement in the measurement of $|V_{ub}|$ from the endpoint spectrum[30].

In addition we have demonstrated useful approximations to the maximum likelihood method that allow us to cope with the limited size of the Monte Carlo samples available to modern high-luminosity experiments. We have also developed the procedures needed to evaluate the corrections and additional uncertainties due to these approximations. These methods are not unique to $B \rightarrow D^* \ell \nu$ or $B \rightarrow J/\psi K^*$ decays, but could be applied to any analysis with a complex multi-dimensional acceptance and resolution functions.

An approach to multi-dimensional goodness-of-fit criteria that allows assessment of the quality of a likelihood fit has also been developed. A binned χ^2 measure, with the method developed to estimate the errors, yields a measure of goodness-of-fit that has a straightforward

statistical interpretation which is easily and intuitively understandable.

XI. ACKNOWLEDGMENTS

The authors wish to thank B. Grinstein, Z. Ligeti, M. Neubert, L. Lellouch and L. Oliver for very useful discussions of the theoretical issues involved in this work.

We are grateful for the extraordinary contributions of our PEP-II colleagues in achieving the excellent luminosity and machine conditions that have made this work possible. The success of this project also relies critically on the expertise and dedication of the computing organizations that support BABAR. The collaborating institutions wish to thank SLAC for its support and the kind hospitality extended to them. This work is supported by the US Department of Energy and National Science Foundation, the Natural Sciences and Engineering Research Council (Canada), Institute of High Energy Physics (China), the Commissariat à l'Énergie Atomique and Institut National de Physique Nucléaire et de Physique des Particules (France), the Bundesministerium für Bildung und Forschung and Deutsche Forschungsgemeinschaft (Germany), the Istituto Nazionale di Fisica Nucleare (Italy), the Foundation for Fundamental Research on Matter (The Netherlands), the Research Council of Norway, the Ministry of Science and Technology of the Russian Federation, and the Particle Physics and Astronomy Research Council (United Kingdom). Individuals have received support from CONACyT (Mexico), the A. P. Sloan Foundation, the Research Corporation, and the Alexander von Humboldt Foundation.

-
- [1] J.E. Duboscq *et al.* (CLEO Collaboration), Phys. Rev. Lett. **76**, 3898 (1996).
- [2] For a theoretical review, see, for example, M. Neubert, “Heavy quark symmetry,” Phys. Rep. **245**, 259 (1994) [arXiv:hep-ph/9306320].
- [3] For a review of semileptonic B decays, see for example, J. D. Richman and P. R. Burchat, “Leptonic and semileptonic decays of charm and bottom hadrons,” Rev. Mod. Phys. **67**, 893 (1995) [arXiv:hep-ph/9508250].
- [4] H. Albrecht *et al.* (ARGUS Collaboration), Z. Phys. C **57**, 533 (1993).
- [5] D. Buskulic *et al.* (ALEPH Collaboration), Phys. Lett. B **359**, 236 (1995).
- [6] D. Buskulic *et al.* (ALEPH Collaboration), Phys. Lett. B **395**, 373 (1997).
- [7] P. Abreu *et al.* (DELPHI Collaboration), Phys. Lett. B **510**, 55 (2001).
- [8] K. Ackerstaff *et al.* (OPAL Collaboration), Phys. Lett. B **395**, 128 (1997).
- [9] The BABAR Collaboration, B. Aubert *et al.*, Phys. Rev. D-RC **71**, 051502 (2005) [arXiv: hep-ex/0408027].
- [10] I. Caprini, L. Lellouch and M. Neubert, “Dispersive bounds on the shape of $\bar{B} \rightarrow D^* \ell \bar{\nu}$ form factors,” Nucl. Phys. B **530**, 153 (1998) [arXiv:hep-ph/9712417].
- [11] C. G. Boyd, B. Grinstein and R. F. Lebed, “Model independent determinations of $\bar{B} \rightarrow D^* \ell \bar{\nu}$ form-factors,” Nucl. Phys. B **461**, 493 (1996) [arXiv:hep-ph/9508211].
- [12] A. Le Yaouanc, L. Oliver and J. C. Raynal, “Bounds on the derivatives of the Isgur-Wise function from sum rules in the heavy quark limit of QCD,” Phys. Lett. B **557**, 207 (2003) [arXiv:hep-ph/0210231]; A. Le Yaouanc, L. Oliver and J. C. Raynal, “Sum rules in the heavy quark limit of QCD,” Phys. Rev. D **67**, 114009 (2003) [arXiv:hep-ph/0210233].
- [13] N. Isgur and M. B. Wise, “Weak transition form-factors between heavy mesons,” Phys. Lett. B **237**, 527 (1990).
- [14] B. Grinstein and Z. Ligeti, “Heavy quark symmetry in $\bar{B} \rightarrow D^* \ell \bar{\nu}$ spectra,” Phys. Lett. B **526**, 345 (2002) [Erratum-ibid. B **601**, 236 (2004)] [arXiv:hep-ph/0111392].
- [15] F. E. Close and A. Wambach, “Quark model form-factors for heavy quark effective theory,” Nucl. Phys. B **412**, 169 (1994) [arXiv:hep-ph/9307260].
- [16] The BABAR Collaboration, B. Aubert *et al.*, Nucl. Instrum. Methods A **479**, 1-116 (2002).
- [17] S. Agostinelli *et al.*, Geant4 Collaboration, Nucl. Instrum. Methods A **506**, 250-302 (2003).
- [18] D. Lange, Nucl. Instrum. Methods A **462**, 152-155 (2001).
- [19] A. Ryd, Ph.D. Thesis, University of California, Santa Barbara (UCSB), UMI-97-04221-mc (microfiche), (1996).
- [20] S. Jadach, B. F. L. Ward and Z. Was, “The precision Monte Carlo event generator KK for two-fermion final states in $e^+ e^-$ collisions,” Comput. Phys. Commun. **130**, 260-325 (2000) [arXiv:hep-ph/9912214].
- [21] E. Richter-Was, “QED bremsstrahlung in semileptonic B and leptonic tau decays,” Phys. Lett. B **303**, 163 (1993).
- [22] Review of Particle Physics, S. Eidelman *et al.*, Phys. Lett. B **592**, 1 (2004) [http://pdg.lbl.gov].
- [23] “Measurement of the $B \rightarrow J/\psi K^*$ (892) Decay Amplitudes,” by the BABAR Collaboration, Phys. Rev. Lett. **87**, 241801 (2001) [arXiv:hep-ex/0107049].
- [24] M. S. Gill, Ph.D. Thesis, University of California, Berkeley (UCB), (2004) [SLAC Report 794: <http://www.slac.stanford.edu/cgi-wrap/pubpage?SLAC-R-794>].
- [25] The BABAR Collaboration, B. Aubert *et al.*, “Ambiguity-free measurement of $\cos(2\beta)$: Time-integrated and time-dependent angular analyses of $B \rightarrow J/\psi K \pi$,” Phys. Rev. D **71**, 032005 (2005).
- [26] R. J. Barlow and C. Beeston, “Fitting using finite Monte Carlo samples,” Comput. Phys. Commun. **77**, 219 (1993).
- [27] A. Le Yaouanc, L. Oliver and J. C. Raynal, “Lower bounds on the curvature of the Isgur-Wise function,” Phys. Rev. D **69**, 094022 (2004) [arXiv:hep-ph/0307197].
- [28] H. Chernoff and E. L. Lehman, Ann. Math. Stat. **25**, 579-586 (1954).
- [29] Z. Ligeti, private communication, May 2005.
- [30] The BABAR Collaboration, B. Aubert *et al.*, “Measurement of the inclusive electron spectrum in charmless B decays near the kinematic endpoint and determination of $|V(ub)|$,” to be published in Phys. Rev. D **73**, 012066 (2006) [arXiv:hep-ex/0509040].
- [31] “Measurement of $B \rightarrow D^*$ Form Factors in the Semileptonic Decay $B^0 \rightarrow D^{*-} \ell^+ \nu$,” by the BABAR Collaboration, submitted to ICHEP 2004 [arXiv:hep-ex/0409047].

Appendix A: Evaluation of additional errors

We supply here some of the mathematical details associated with biases and uncertainties introduced in our application of the maximum likelihood method. See Ref. [24] for further details.

Except as noted, in the below, we use the notation of Sec. VI.

1. Bias From Approximate PDF

Suppose events are distributed as

$$\frac{\mathcal{F}(x; \mu_t)}{\int dx \mathcal{F}(x; \mu_t)}, \quad (56)$$

but the unnormalized PDF used in the maximum likelihood fit is $f(x; \mu)$ (defined by Eq.(30) and used as an

approximation for the unknown $\mathcal{F}(\tilde{x}; \mu)$ in Eq. (31)). As the number of events N tends to infinity, the sum defining the likelihood can be replaced by the integral

$$\ln L = N \int dx \mathcal{F}(x; \mu_t) \ln f(x; \mu) - N \ln \int dx f(x; \mu). \quad (57)$$

The second term comes from normalizing the PDF. If we expand about μ_t and keep only the leading terms, treating

$$\frac{\mathcal{F}(x; \mu_t)}{\int dx \mathcal{F}(x; \mu_t)} - \frac{f(x; \mu_t)}{\int dx f(x; \mu_t)} \quad (58)$$

as being itself of order $\mu - \mu_t$, we find that the maximum occurs at the point where the derivatives given by

$$\frac{\partial}{\partial \mu} \ln L = \int dx \mathcal{F}(x; \mu_t) \frac{\partial}{\partial \mu} \ln f \left(\frac{\mathcal{F}(x; \mu_t)}{\int dx \mathcal{F}(x; \mu_t)} - \frac{f(x; \mu_t)}{\int dx f(x; \mu_t)} \right) + \left(\left\langle \frac{\partial \ln f}{\partial \mu} \right\rangle \left\langle \frac{\partial \ln f}{\partial \mu} \right\rangle^T - \left\langle \left\langle \frac{\partial \ln f}{\partial \mu} \right\rangle \left(\frac{\partial \ln f}{\partial \mu} \right)^T \right) (\mu - \mu_t) \quad (59)$$

are zero. All derivatives are evaluated at $\mu = \mu_t$.

When we take the approximation

$$f(x; \mu) = \mathcal{F}(x; \mu_{\text{mc}}) \frac{F(x; \mu)}{F(x; \mu_{\text{mc}})} \quad (60)$$

and expand about $\mu = \mu_t$, we find to leading order

$$\frac{\mathcal{F}(x; \mu_t)}{\int dx \mathcal{F}(x; \mu_t)} - \frac{f(x; \mu_t)}{\int dx f(x; \mu_t)} = \frac{\mathcal{F}(x; \mu_t)}{\int dx \mathcal{F}(x; \mu_t)} \left[\left\langle \frac{\partial \ln \frac{\mathcal{F}}{F}}{\partial \mu} \right\rangle - \frac{\partial \ln \frac{\mathcal{F}}{F}}{\partial \mu} \right]^T (\mu_{\text{mc}} - \mu_t). \quad (61)$$

Setting the derivative of the log-likelihood to zero, we have

$$\begin{aligned} (\mu_{\text{mc}} - \mu_t) \left[\left\langle \frac{\partial \ln \frac{\mathcal{F}}{F}}{\partial \mu} \right\rangle \left\langle \frac{\partial \ln F}{\partial \mu} \right\rangle^T - \left\langle \left(\frac{\partial \ln \frac{\mathcal{F}}{F}}{\partial \mu} \right) \left(\frac{\partial \ln F}{\partial \mu} \right)^T \right\rangle \right]^T = \\ -(\mu - \mu_t) \left[\left\langle \frac{\partial \ln F}{\partial \mu} \right\rangle \left\langle \frac{\partial \ln F}{\partial \mu} \right\rangle^T - \left\langle \left(\frac{\partial \ln F}{\partial \mu} \right) \left(\frac{\partial \ln F}{\partial \mu} \right)^T \right\rangle \right]^T. \end{aligned} \quad (62)$$

Solving for the bias $\mu - \mu_t$ yields the result Eq.(34).

2. Error from Monte Carlo evaluation of normalization

The error induced by the use of Monte Carlo integration to normalize a PDF can be calculated considering the asymptotic form

$$\ln L = N \int dx f(x; \mu_t) \ln f(x; \mu) - N \ln \left[\int f(x; \mu) dx + \epsilon(\mu) \right] \quad (63)$$

where now we are no longer concerned with the distinction between \mathcal{F} and f . The function $\epsilon(\mu)$ is the deviation of the Monte Carlo integral from the true integral. The maximization equation now reads

$$\frac{\partial}{\partial \mu} \ln L = \left(\left\langle \frac{\partial \ln f}{\partial \mu} \right\rangle \left\langle \frac{\partial \ln f}{\partial \mu} \right\rangle^T \left\langle \left(\frac{\partial \ln f}{\partial \mu} \right) \left(\frac{\partial \ln f}{\partial \mu} \right)^T \right\rangle \right) (\mu - \mu_t) - \frac{\partial}{\partial \mu} \frac{\epsilon(\mu)}{\int dx f(x; \mu)}, \quad (64)$$

so, again setting the log of the likelihood to zero, the bias is

$$(\mu - \mu_t) = - \frac{\partial}{\partial \mu} \frac{\epsilon(\mu)}{\int dx f(x; \mu)} E, \quad (65)$$

where we recognize that the term multiplying $(\mu - \mu_t)$ in Eq.(64) is the inverse of the error matrix E .

Now we suppose the Monte Carlo simulation to be accurate so there is no bias, but an uncertainty is introduced by the fluctuations in ϵ . We therefore need an estimate of the matrix

$$\left\langle \left(\frac{\partial}{\partial \mu_\alpha} \frac{\epsilon(\mu)}{\int dy f(y; \mu)} \right) \left(\frac{\partial}{\partial \mu_\beta} \frac{\epsilon(\mu)}{\int dy' f(y'; \mu)} \right)^T \right\rangle. \quad (66)$$

A straightforward calculation gives

$$\begin{aligned} & \frac{1}{(\int dx f)^2} \int dx \left(\frac{\partial f}{\partial \mu} \right) \left(\frac{\partial f}{\partial \mu} \right)^T \\ & - \frac{1}{(\int dx f)^3} \left[\left(\int dx \frac{\partial f}{\partial \mu} \right) \left(\int dx f \frac{\partial f}{\partial \mu} \right)^T + \left(\int dx f \frac{\partial f}{\partial \mu} \right) \left(\int dx \frac{\partial f}{\partial \mu} \right)^T \right] \\ & + \frac{1}{(\int dx f)^4} \left(\int dx \frac{\partial f}{\partial \mu} \right) \left(\int dx \frac{\partial f}{\partial \mu} \right)^T \int dx f^2. \end{aligned} \quad (67)$$

To apply this to our circumstance where we perform a Monte Carlo integration with points having the density $\mathcal{F}(x; \mu_{mc})$, we need to make the identifications

$$\frac{1}{N_{MC}} \sum_i \dots \rightarrow \frac{1}{\int dx \mathcal{F}} \int dx \mathcal{F}(x; \mu_{mc}) \dots; \quad f \rightarrow \frac{F(x; \mu)}{F(x; \mu_{mc})}. \quad (68)$$

In the final expressions, we do not need to make the distinctions between μ , μ_{mc} , and μ_t which is only necessary when taking the derivatives with respect to μ . These differences are of higher order. This results in the correspondences

$$\int dx f \rightarrow \int dx \mathcal{F}(x; \mu_t) \quad (69)$$

$$\int dx \frac{\partial f}{\partial \mu} \rightarrow \int dx \mathcal{F}(x; \mu_t) \frac{\partial \ln F(x; \mu)}{\partial \mu} = \left\langle \frac{\partial \ln F}{\partial \mu} \right\rangle \int dx \mathcal{F}, \text{ etc.} \quad (70)$$

$$(71)$$

where the derivatives are evaluated at μ_t

In this way we find

$$\begin{aligned} \left\langle \left(\frac{\partial}{\partial \mu_\alpha} \frac{\epsilon(\mu)}{\int dy f(y; \mu)} \right) \left(\frac{\partial}{\partial \mu_\beta} \frac{\epsilon(\mu)}{\int dy' f(y'; \mu)} \right)^T \right\rangle &= \frac{1}{M_{MC}} \left\langle \left(\frac{\partial \ln F}{\partial \mu} \right) \left(\frac{\partial \ln F}{\partial \mu} \right)^T \right\rangle - \left\langle \frac{\partial \ln F}{\partial \mu} \right\rangle \left\langle \frac{\partial \ln F}{\partial \mu} \right\rangle^T \\ &= \frac{1}{M_{MC}} E^{-1} \end{aligned} \quad (72)$$

and

$$\left\langle (\mu - \mu_t) (\mu - \mu_t)^T \right\rangle = E \frac{1}{M_{MC}} E^{-1} E = \frac{1}{M_{MC}} E, \quad (73)$$

where $M_{MC} = N_{MC}/N_{data}$ is the ratio between the number of MC events and the number of signal events in the

data (the inverse of the r_{mc} used in Sec. VIII). That is to

say, the error matrix due to Monte Carlo integration has the same form as that for the statistical error from data, except that it is $1/N_{MC}$ instead of $1/N_{\text{data}}$ that enters.

3. Pseudo-log-likelihood Error

The pseudo-log-likelihood error can be computed from sums over the Monte Carlo sample used in the background subtraction. In this case the weights (w_i) are those used to weight each type of background to obtain the correct normalization as described in Sec. VIC (see Eq. (42)).

We consider a pseudo-log-likelihood

$$\begin{aligned} \ln A = & \sum_{i(S)} \ln F_S(x_i; \mu) + \sum_{j(B)} \ln F_S(x_j; \mu) \\ & - \sum_{j'(B,MC)} \ln F_S(x_{j'}; \mu) - N_S \int dx F_S(x; \mu) \end{aligned} \quad (74)$$

where the S , B , and (B, MC) indicate that the sums are over signal events, background events, and background MC events, respectively. Of course we cannot know event-by-event which are signal and which are background events, but for the sum this doesn't matter. The signal distribution is indicated by $F_S(x; \mu)$; the background is $F_B(x)$. We expand about $\mu = \mu_t$ and set $(\partial/\partial\mu_\alpha) \ln A$ to zero to find the background subtraction error E_S is given by

$$\begin{aligned} N_S E_S^{-1}(\mu - \mu_t) = & \sum_{i(S)} \frac{\partial}{\partial\mu} \delta \ln F_S(x_i; \mu) \\ & + \sum_{j(B)} \frac{\partial}{\partial\mu} \delta \ln F_S(x_j; \mu) \\ & - \sum_{j'(B,MC)} \frac{N_B}{N_{MC}} \frac{\partial}{\partial\mu} \delta \ln F_S(x_{j'}; \mu) \end{aligned} \quad (75)$$

where

$$\delta \ln F_S(x_i; \mu) = \ln F_S(x_i; \mu) - \frac{\int dx F_S(x; \mu_t) \ln F_S(x; \mu)}{\int dx F_S(x; \mu_t)}, \quad (76)$$

and

$$\begin{aligned} E_S^{-1} = & \left\langle \left(\frac{\partial \ln F_S}{\partial \mu} \right) \left(\frac{\partial \ln F_S}{\partial \mu} \right)^T \right\rangle_S \\ & - \left\langle \frac{\partial \ln F_S}{\partial \mu} \right\rangle_S \left\langle \frac{\partial \ln F_S}{\partial \mu} \right\rangle_S^T \end{aligned} \quad (77)$$

where

$$\langle A \rangle_S = \int dx F_S(x; \mu_t) A(x) / \int dx F_S(x; \mu_t) \quad (78)$$

The fluctuations average to zero, but their squares do not. For example,

$$\sum_{i(S)} \sum_{i'(S)} \left(\frac{\partial}{\partial\mu} \delta \ln F_S(x_i; \mu_t) \right) \left(\frac{\partial}{\partial\mu} \delta \ln F_S(x_{i'}; \mu_t) \right)^T = \quad (79)$$

$$N_S \left[\left\langle \left(\frac{\partial \delta \ln F_S}{\partial \mu} \right) \left(\frac{\partial \delta \ln F_S}{\partial \mu} \right)^T \right\rangle_S - \left\langle \frac{\partial \delta \ln F_S}{\partial \mu} \right\rangle_S \left\langle \frac{\partial \delta \ln F_S}{\partial \mu} \right\rangle_S^T \right];$$

$$\sum_{j(B)} \sum_{j'(B)} \left(\frac{\partial}{\partial\mu} \delta \ln F_S(x_j; \mu_t) \right) \left(\frac{\partial}{\partial\mu} \delta \ln F_S(x_{j'}; \mu_t) \right)^T =$$

$$N_B \left[\left\langle \left(\frac{\partial \delta \ln F_S}{\partial \mu} \right) \left(\frac{\partial \delta \ln F_S}{\partial \mu} \right)^T \right\rangle_B - \left\langle \frac{\partial \delta \ln F_S}{\partial \mu} \right\rangle_B \left\langle \frac{\partial \delta \ln F_S}{\partial \mu} \right\rangle_B^T \right] \quad (80)$$

where now

$$\langle A \rangle_B = \int dx F_B(x; \mu_t) A(x) / \int dx F_B(x; \mu_t). \quad (81)$$

Altogether we find

$$\begin{aligned} \langle (\mu - \mu_t)(\mu - \mu_t)^T \rangle &= \frac{1}{N_S} E_S \\ &+ \frac{1}{N_S} \frac{N_B}{N_S} \left(1 + \frac{N_B}{N_{MC}} \right) E_S E_B^{-1} E_S. \end{aligned} \quad (82)$$

Appendix B: Background estimation

This appendix gives more detail on the background estimation procedures.

1. Combinatorial background

Figure 16 shows the distribution of Δm for the data sample on a linear scale. The linear scale is used so the level of combinatorial background can be judged by eye from the tail extending outwards towards the right (the peaking backgrounds are underneath the signal peak here and their levels cannot be distinguished from the data). The combinatorial background appears to be of order 5%, but it is hidden under a signal that has substantial tails. It is difficult to distinguish tail from background. To extract the background fraction and estimate the signal this distribution is fit to a set of Gaussians representing the signal and to a threshold function to model the background. To investigate the background shape and the tails of the signal Monte Carlo simulated events are used.

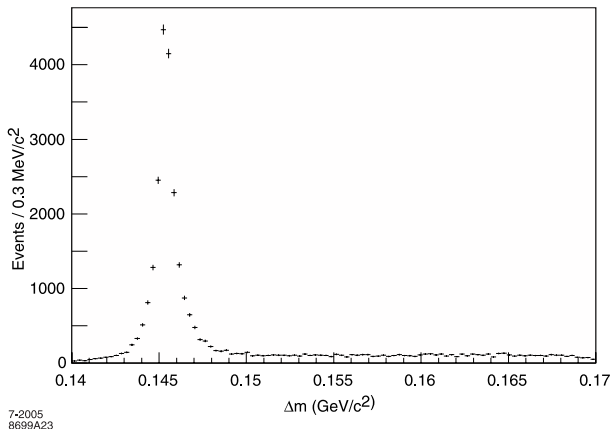


FIG. 16: The Δm data distribution for $D^* e\nu$ candidates on a linear scale.

First, to investigate the shape needed to describe the background, a pure combinatorial background sample selected from the Monte Carlo simulation is used.

Figure 17 shows the distribution of Monte Carlo combinatorial background events fit to the (a) unextended (b) and extended threshold function, as discussed in Sec. VIC1. Though not immediately obvious by eye, the unextended function systematically underestimates the data in the signal region near $\Delta m = 0.1454 \text{ GeV}/c^2$. The true number in the signal box ($0.143 \leq \Delta m \leq 0.148 \text{ GeV}/c^2$) is 3540. The unextended fit yields 3400 ± 39 whereas the extended fit yields the much closer result 3528 ± 52 . Fits to subsets of the Monte Carlo data (*e.g.*, those binned in the kinematic variables) show the same pattern with the fit to the extended function having much better success at estimating the number of background events than the unextended.

Next, Figure 18a shows the Δm distribution of a Monte Carlo simulated pure D^* signal sample. There are substantial tails and even the core is not consistent with a single Gaussian. It takes five Gaussians to achieve the good fit shown in Figure 18a.

The fit to the full MC Δm distribution is finally shown in Figure 18b. In this fit the three core Gaussians of the signal are allowed to float, but the tail is fixed. For the threshold function, the threshold and the scale factor are fixed while the other two parameters are fitted. This procedure reproduces the Monte Carlo input signal and background fractions.

The Δm distribution of the data with the fit as described is shown in Figure 7. We find $N_{cb}^{fit} = 1325 \pm 65$ which corresponds to a combinatorial background fraction of $6.4 \pm 0.3\%$ before cutting on $\cos\theta_{BY}$.

To check the stability of this fit, the fitting conditions are varied. Letting the fourth Gaussian float yields 1374 ± 92 . The error on the difference is ± 65 , so this is consistent with the fixed fourth Gaussian used for the central value. Moving the long tail represented by the fifth Gaussian up and down by 50% results in a variation of $\approx \pm 26$ in the background estimate. This variation is added in quadrature with the error reported by the fit to yield a total error of ± 70 . The combinatorial background fraction with error becomes $6.39 \pm 0.32\%$.

2. Fits in kinematic variable bins

To estimate the difference in kinematic-variable dependence between data and MC, bin-by-bin fits in five bins for each of the four kinematic variables are done. In the five-bin fits for the combinatorial-background kinematic-variable dependence (as discussed in Sec. VIC1) it is found that only four Gaussians are needed to represent the signal shape and that the $\pm 50\%$ variation of the tail Gaussian produces negligible changes in the estimated background level. The Δm plots with fits are shown in Figure 19. The data-to-Monte Carlo ratio plots which result from these fits is shown Fig. 9 in Section VI.

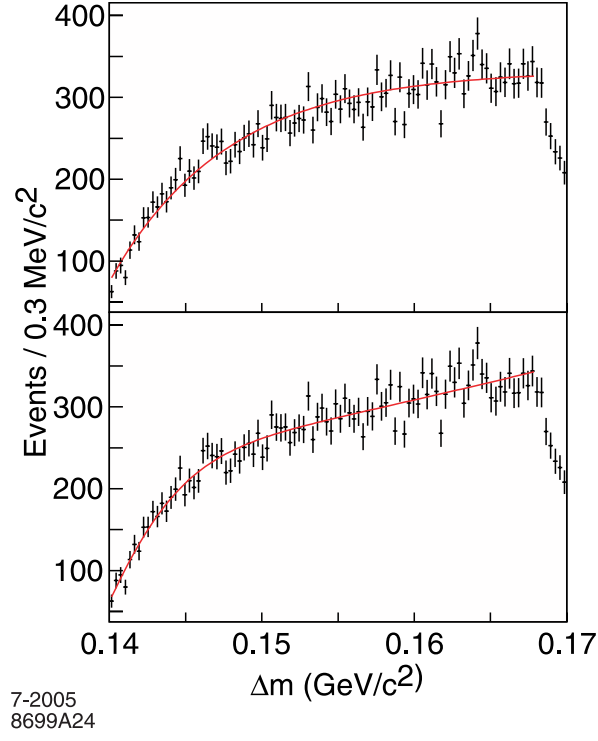


FIG. 17: The Δm distribution for combinatorial background selected from the Monte Carlo with fit to the unextended threshold function (a) and to the extended function.

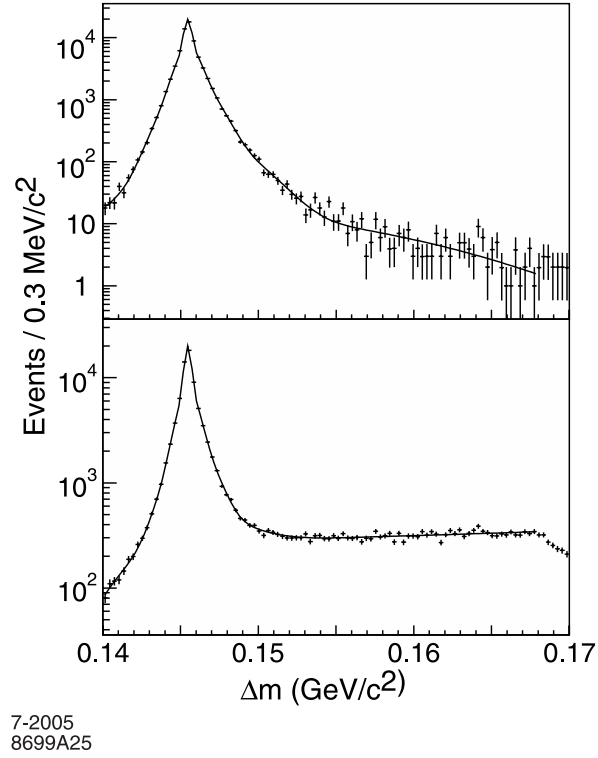


FIG. 18: The Δm distribution for (a) pure D^* signal selected from the Monte Carlo with fit to five Gaussians and (b) the Δm distributions on the full Monte Carlo sample, fit to the five Gaussian signal shape plus extended threshold function.

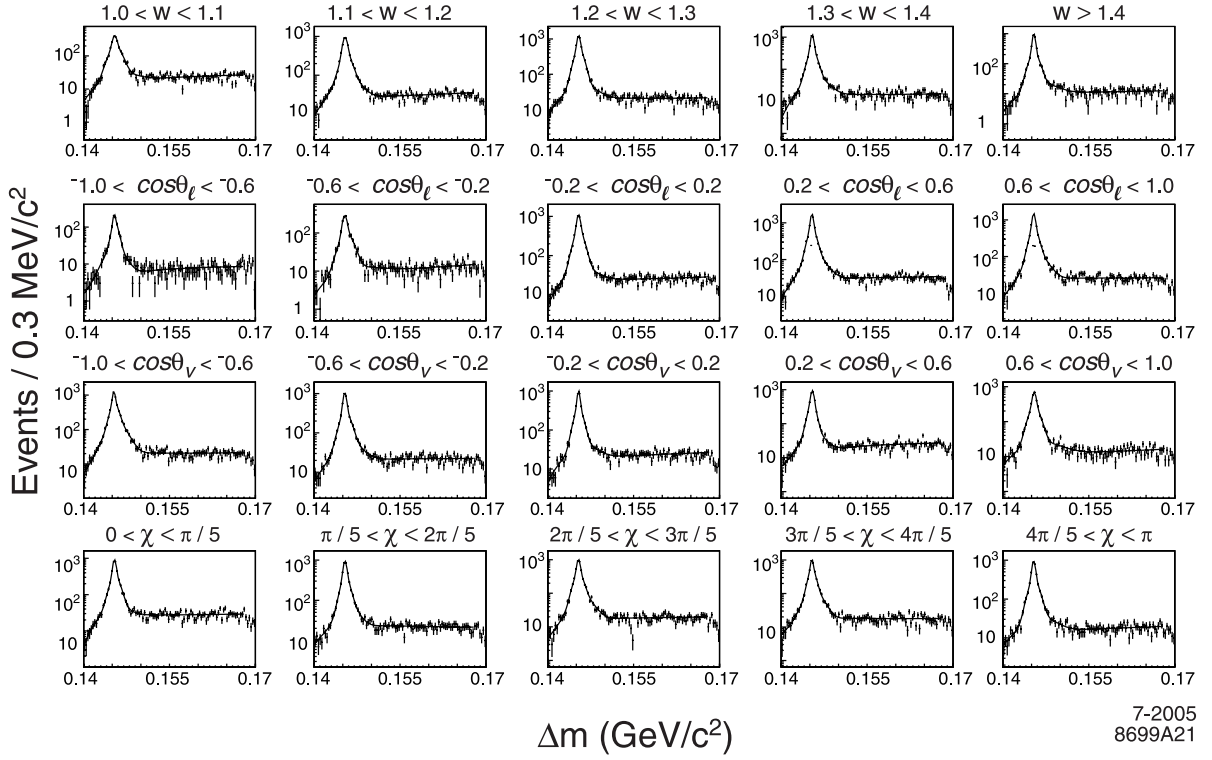


FIG. 19: The Δm distribution for data in kinematic variable bins. The rows are fits for w , $\cos\theta_\ell$, $\cos\theta_V$ and χ in each of the five bins spanning the full range of the variable.

3. Peaking background including D^{**} background fits.

Similarly, $\cos\theta_{BY}$ fits in five bins for each of the four kinematic variables are done to extract the shape of the

D^{**} background. The results of each fit are shown in Figure 20. The data-to-Monte Carlo ratio used to weight the background obtained from these fits are shown in Figure 10 in Section VI.

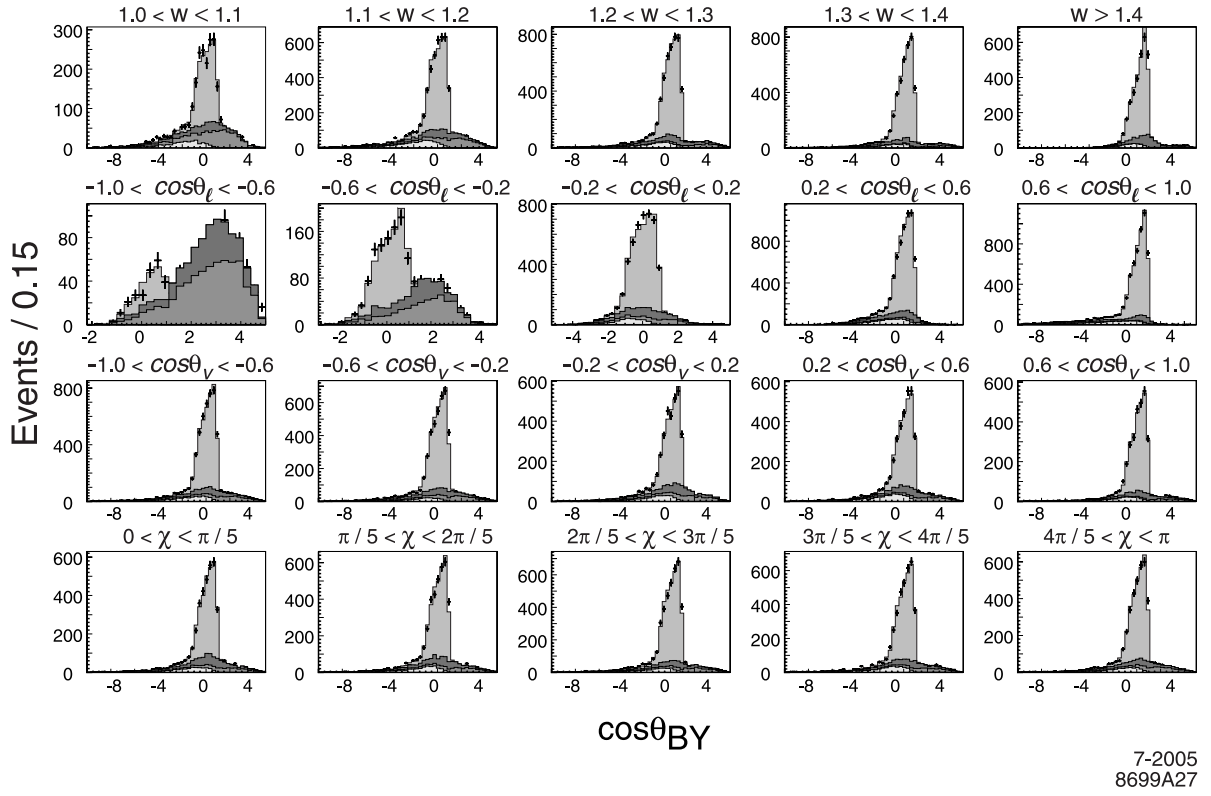


FIG. 20: The $\cos\theta_{BY}$ distributions fit to background plus signal in five bins in each of the kinematic variables. Each row shows the plots for the five bins corresponding to the variables w , $\cos\theta_\ell$, $\cos\theta_V$ and χ . The shading is the same as that in Figure 10.